Computer Methods in Applied Mechanics and Engineering 457 (2026) 118983

Contents lists available at ScienceDirect

Comput. Methods Appl. Mech. Engrg.

journal homepage: www.elsevier.com/locate/cma

A unified topology optimization framework for dynamic contact and friction via hybrid MPM

Isamu Hashiguchi [a], Jike Han [b], Shunsuke Kobayashi [a], Takamitsu Sasaki [b], Ryuichi Tarumi [a,*]

[a] *Graduate School of Engineering Science, The University of Osaka, 1-3 Machikaneyama, Toyonaka, 560-8531, Osaka, Japan*
[b] *Department of Mechanical Engineering and Science, Kyoto University, Kyoto-daigaku Katsura C3, Nishikyo-ku, Kyoto, 615-8540, Kyoto, Japan*

ARTICLE INFO

Keywords:
Topology optimization
Material point method
Dynamical contact
Coulomb friction
Compliant mechanical systems
Energy dissipating devices

ABSTRACT

This study introduces a unified topology optimization (TO) framework capable of handling dynamic mechanical contact with interfacial friction between deformable bodies. The approach leverages a hybrid material point method (MPM), whose mathematical structure closely parallels that of classical finite element analysis, enabling a natural and consistent extension of well-established TO formulations. Through the MPM mapping operation, the framework accurately captures contact dynamics and provides a robust stick–slip formulation of Coulomb friction. Sensitivities are computed using the adjoint method with automatic differentiation, and optimal configurations are iteratively updated via the method of moving asymptotes. The compliance minimization of a three-point bending setting and the energy minimization of a contacting body demonstrate that the proposed framework remains robust for complex dynamics with large, time-evolving changes in contact interfaces and with frictional responses that directly influence overall deformation behavior. The robustness of the present framework is further demonstrated through its successful extension to fully three-dimensional settings. These results convincingly demonstrate that the hybrid MPM-based TO substantially advances structural optimization by directly incorporating dynamic contact with friction, thereby providing a unified framework for designing energy-dissipating compliant mechanical systems and devices.

1. Introduction

In recent years, considerable progress has been made in soft robotics, which exploits the mechanical compliance of soft materials [1,2]. Key functions such as impact absorption [3,4] and gripping [5,6] critically rely on large deformations, where geometric nonlinearity fundamentally governs the mechanical response. In addition, many soft robotic components operate under dynamic loading conditions, where inertia, rate, and time-dependent effects play a decisive role. In such settings, mechanical contact is not static but evolves continuously in time, often accompanied by separation, re-contact, and frictional slip. Eventually, the overall behavior becomes highly nonlinear and history-dependent.

Despite these intrinsic nonlinearities, the design of soft robotic structures is still frequently guided by empirical rules, intuition, or incremental modifications of existing prototypes. However, when large deformations, evolving contact interfaces, and frictional interactions under dynamic loading are involved, the mechanical response arises from a highly coupled interplay between geometry, material distribution, inertia, and contact mechanics, making purely heuristic approaches insufficient. To address this complexity,

* Corresponding author.
E-mail address: tarumi.ryuichi.es@osaka-u.ac.jp (R. Tarumi).

https://doi.org/10.1016/j.cma.2026.118983
Received 26 November 2025; Received in revised form 19 March 2026; Accepted 9 April 2026
Available online 20 April 2026

systematic and physics-based design methodologies are required. Among the promising candidates, topology optimization (TO) [7] has attracted considerable attention as a computational framework for determining optimal material distributions within a prescribed domain under governing mechanical constraints, providing a rational and mechanics-based alternative to intuition-driven design. However, the simultaneous treatment of “finite deformation”, “inertial effect”, and “contact interaction” within a unified TO framework has not yet been fully established and remains a significant open challenge.

Extensive research efforts have been devoted to finite strain TO, where geometric nonlinearity plays a central role in the structural response. Early work by Buhl et al. [8] highlighted the role of geometric nonlinearity, and Bruns & Tortorelli [9] demonstrated nonlinear optimal designs using the St.Venant–Kirchhoff model. Kang & Luo [10] formulated a non-probabilistic reliability-based finite strain TO method. Subsequent developments include additive hyperelasticity for mitigating distortion in low-density regions [11], discrete sensitivity analysis for finite strain elastoplasticity [12], optimal fiber orientation in hyperelastic composites [13], and TO frameworks for hyperelastic structures with anisotropic fiber reinforcement [14]. Han et al. [15] further extended TO to multi-material elastoplastic systems under finite strain.

Similarly, TO for dynamic problems has been actively investigated, incorporating inertial effects or time-dependent responses into the design formulation. Min et al. [16] pioneered this direction by presenting a TO framework for elastic structures under dynamic loads. Subsequent studies improved computational efficiency through equivalent static load-based approaches [17], extended the objective functions to suppress maximum transient responses [18], introduced fully time-dependent adjoint sensitivity analysis for more accurate gradient evaluation [19], and further expanded the framework to nonlinear elastic settings [20,21]. More recently, Kristiansen et al. [22] extended dynamic TO to transient impact problems with friction.

In addition, TO involving mechanical contact has attracted growing attention for addressing challenges such as unilateral constraints, sliding interfaces, and frictional interactions. Notable contributions include contact-aided compliant mechanisms [23], mass minimization with Coulomb friction [24], unilateral contact formulations using augmented Lagrangians [25], sliding and separation in two-phase systems [26], frictional contact via regularized Coulomb models [27], and frictional-contact TO using p-norm objectives and Lagrange multipliers [28]. Recent advances addressing both nonlinearities and contact include automated synthesis of compliant mechanisms [29], hyperelastic TO with frictionless contact supports [30], large-deformation contact between multiple deformable bodies [31], self-contact methods based on a third-medium formulation [32,33], and hyperelastic TO under large-deformation, frictionless contact [34].

While substantial progress has been made in addressing finite deformation, inertia, and contact individually in TO, no prior study has yet integrated all three aspects within a unified framework. For example, although several studies have already incorporated inertia effects into finite strain TO, allowing the optimal configuration to evolve under dynamic loading [20,21], these formulations have not yet extended to explicitly account for contact interaction. A primary reason lies in the inherent difficulty of contact modeling: conventional finite element-based approaches rely on explicit contact detection, requiring repeated nearest-neighbor searches between opposing interfaces [35,36]. Such procedures can become computationally expensive, particularly in dynamic problems where the active contact set evolves continuously, and pose a significant obstacle to robust large-scale optimization. As a countermeasure, detection-free formulations have recently been explored to mitigate this limitation. For instance, the Third Medium Contact (TMC) method [37] eliminates explicit contact search by introducing a virtual compressible layer and has been successfully applied to static TO problems [32,33,38]. However, in dynamic scenarios involving large sliding or rotation, severe distortion of the intermediate medium may impair numerical robustness [33]. Similarly, the Material Point Method (MPM) [39] mediates interaction through a fixed Eulerian grid, thereby avoiding explicit detection and mesh distortion, and has recently been adopted in TO of soft robotic structures [40–44]. Nevertheless, its potential has not yet been fully exploited for general deformable-deformable contact, partly due to issues such as nonphysical adhesion and the nontrivial incorporation of friction.

Based on the above background, the present study proposes a unified TO framework capable of consistently treating finite deformation, inertial effects, and contact interaction among multiple deformable continua. Specifically, the Hybrid Material Point Method (Hybrid-MPM) [45], which combines the strengths of FEM and conventional MPM, is employed as the underlying analysis tool. This approach enables a contact formulation independent of predefined interface configurations and capable of handling arbitrary mutual contact within a single computational framework. By utilizing a fixed Eulerian background grid, it circumvents explicit contact detection, avoids the nonphysical adhesion inherent to conventional MPM, and allows consistent incorporation of a Coulomb friction law. A key contribution of this work is the construction of a general contact-enabled formulation together with a systematic and problem-independent sensitivity analysis. Adjoint-based sensitivities are derived in a unified manner, such that the resulting formulation is not tailored to a specific application but can be directly applied to a broad class of nonlinear dynamic contact problems. As a proof of concept, the framework is applied to optimization problems that have not previously been addressed within TO, including mechanisms designed to control rotational motion under large deformation and contact interaction. Through these developments, the present study establishes a comprehensive and extensible computational foundation for contact-inclusive dynamic TO.

The remainder of this paper is organized as follows. Section 2 presents the theory of the differentiable Hybrid MPM, which enables the appropriate evaluation of the sensitivities required for topology optimization. Section 3 then introduces the formulation of the optimization problem and presents a sensitivity analysis method for generalized dynamic analysis, thereby deriving the sensitivity evaluation procedure for the Hybrid MPM. Section 4 verifies the effectiveness of the present framework through two optimization examples: the compliance minimization problem of three-point bending and the optimization of a brake structure for suppressing the kinetic energy of a rotating sphere. Finally, Section 5 presents the concluding remarks.

2. Dynamic contact analysis with interfacial friction

2.1. Finite element discretization for the equation of motion

We outline the hybrid MPM as the mathematical foundation for the structural analysis employed in the present TO framework. The standard MPM is a particle-based method in which a solid is discretized into Lagrangian material points. Mapping the particle velocities onto an Eulerian background grid enables contact interactions to be handled without the need for explicit contact detection [46–49]. However, this particle-based approximation inherently limits the accurate representation of boundary geometry, which, in turn, restricts comprehensive frictional contact analysis. In contrast, the hybrid MPM discretizes the solid using finite elements (FE), allowing boundary geometry and normal directions to be obtained explicitly through the shape functions [45], while critically retaining the MPM-based velocity mapping for robust contact handling [46]. These combined features establish the hybrid MPM as a natural and accurate foundation for contact mechanics within topology optimization. A concise overview is provided below for clarity.

Fig. 1(a) schematically illustrates a dynamic problem involving mechanical contact between two deformable bodies. For later convenience, we denote the design domain by Ω_0 and the contacting object by Ω_0'. For simplicity, we describe the equation of motion only for the body Ω_0; essentially the same formulation applies to Ω_0'. Let the body Ω_0 be in a stress-free reference configuration at the initial time $t = 0$, and let $\boldsymbol{X} \in \Omega_0$ denote the material coordinate. The kinematics of the body are described by a smooth motion map such that $\boldsymbol{X} \mapsto \boldsymbol{x}$, where $\boldsymbol{x}$ is the current spatial coordinate at time t. The displacement can then be written as $\boldsymbol{u} = \boldsymbol{x} - \boldsymbol{X}$. We assume that the deformation gradient $\boldsymbol{F} = \partial \boldsymbol{x}/\partial \boldsymbol{X}$ is well-defined at any time t throughout the domain Ω_0. The boundary Γ of the body Ω_0 is decomposed into a Dirichlet boundary Γ_D and a Neumann boundary Γ_N, satisfying $\Gamma = \Gamma_D \cup \Gamma_N$ and $\Gamma_D \cap \Gamma_N = \emptyset$. A prescribed surface traction $\boldsymbol{t}_0$ may act on Γ_N in the reference configuration. It should be noted that this surface traction is distinct from the contact force arising between the deformable bodies, which is introduced through the MPM mapping and is described in the next section. The spatially discretized equation of motion for the FEM simulation is given by [50,51]

$$m_\alpha \ddot{\boldsymbol{x}}_\alpha = \boldsymbol{f}_\alpha^{\text{int}} + \boldsymbol{f}_\alpha^{\text{ext}}, \tag{1}$$

where a superposed dot $(\dot{\ })$ denotes the time derivative; for example, $\dot{\boldsymbol{x}} = \boldsymbol{v}$ and $\ddot{\boldsymbol{x}} = \boldsymbol{a}$ represent the velocity and acceleration. m_α denotes the lumped mass [52,53] associated with the node α. Hereafter, the subscript α denotes the quantity associated with node α. The terms $\boldsymbol{f}_\alpha^{\text{int}}$ and $\boldsymbol{f}_\alpha^{\text{ext}}$ represent the internal and external nodal forces, respectively. They are explicitly defined as

$$m_\alpha = \int_{\Omega_0} \rho_0 K_\alpha dV, \quad \boldsymbol{f}_\alpha^{\text{int}} = -\int_{\Omega_0} \boldsymbol{P}(\boldsymbol{u}) \frac{\partial K_\alpha}{\partial \boldsymbol{X}} dV, \quad \boldsymbol{f}_\alpha^{\text{ext}} = \int_{\Omega_0} \boldsymbol{b}_0 K_\alpha dV + \int_{\Gamma_N} \boldsymbol{t}_0 K_\alpha d\Gamma, \tag{2}$$

where K_α is a shape function. Although the underlying theory remains valid for shape functions of arbitrary order, we specifically employed first-order functions in the present numerical analysis which satisfy the partition of unity $\sum_{\alpha \in \mathcal{N}_{\text{FA}}} K_\alpha(\boldsymbol{X}) = 1$. ρ_0 and $\boldsymbol{b}_0$ denote the mass density and the body force per unit reference volume, respectively. $\boldsymbol{P} = \partial \varphi / \partial \boldsymbol{F}$ is the first Piola–Kirchhoff stress tensor, obtained as the partial derivative of the strain energy density φ with respect to the deformation gradient $\boldsymbol{F}$. By applying a forward Euler time discretization with time increment Δt, the acceleration $\ddot{\boldsymbol{x}}_\alpha$ in the equation of motion is approximated as $\ddot{\boldsymbol{x}}_\alpha = \left(\boldsymbol{v}_\alpha^{(n+1)} - \boldsymbol{v}_\alpha^{(n)} \right) / \Delta t$, where $\boldsymbol{v}^{(n)}$ denotes the velocity at the nth time step. Consequently, the velocity and current configuration at the next step are updated as follows:

$$\boldsymbol{v}_\alpha^{(n+1)} = \boldsymbol{v}_\alpha^{(n)} + \frac{\Delta t}{m_\alpha} \left(\boldsymbol{f}_\alpha^{\text{int}(n)} + \boldsymbol{f}_\alpha^{\text{ext}(n)} \right), \quad \boldsymbol{x}_\alpha^{(n+1)} = \boldsymbol{x}_\alpha^{(n)} + \Delta t \boldsymbol{v}_\alpha^{(n+1)}. \tag{3}$$

Note that alternative numerical schemes, such as the Newmark-beta or Runge–Kutta methods, are also applicable to this framework. Repeating this procedure yields the full dynamical response of the body. This constitutes the standard explicit FEM scheme for dynamical problems.

2.2. Hybrid MPM for mechanical contact

The hybrid MPM introduces contact effects into the standard FEM formulation through a modification of the updated nodal velocity $\boldsymbol{v}_\alpha^{(n+1)}$ in Eq. (3). For clarity, we refer to this intermediate quantity as the tentative updated velocity and denote it by $\boldsymbol{v}_\alpha^*$, rather than $\boldsymbol{v}_\alpha^{(n+1)}$. The hybrid MPM introduces collision particles (CPs) placed along the FE mesh boundary, requiring interpolation between FE nodes and CPs, and mapping between CPs and Eulerian grids. As illustrated in Fig. 1(b), each time step consists of the following processes:

1. The F2C step interpolates the mass and velocity of the FE nodes to the CPs using the shape function B_α, *i.e.*, $m_\alpha \to m_q$ and $\boldsymbol{v}_\alpha^* \to \boldsymbol{v}_q^*$;
2. The C2G step maps the mass, momentum, and velocity of the CPs to the Eulerian grids using the kernel function ψ, *i.e.*, $m_q \to m_i$ and $\boldsymbol{v}_q^* \to \boldsymbol{v}_i^*$;
3. The G2C step maps the velocity of the Eulerian grids to the CPs using the kernel function ψ, *i.e.*, $\boldsymbol{v}_i^* \to \boldsymbol{v}_q^{**}$; To prevent non-physical numerical adhesion, the velocity difference $\Delta \boldsymbol{v}_q = \boldsymbol{v}_q^{**} - \boldsymbol{v}_q^*$ is evaluated and subsequently modified to $\Delta \boldsymbol{v}_q'$ according to the orientation of relative motion (see Section 2.3 for details);
4. The C2F step interpolates the velocity difference of the CPs to the FE nodes using the shape function B_α, *i.e.*, $\Delta \boldsymbol{v}_q' \to \Delta \boldsymbol{v}_\alpha'$.

This method, originally developed by Han et al. [45], has been confirmed to exhibit good energy conservation properties for the class of problems considered here. The main computational steps of the hybrid MPM scheme are summarized as follows.

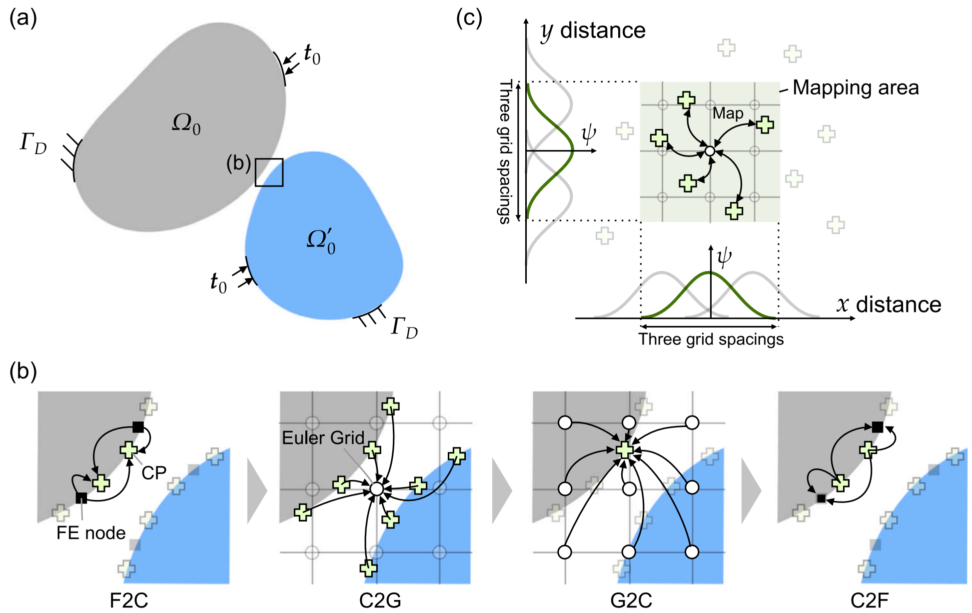

Fig. 1. (a) Schematic of the dynamic contact problem, showing the geometry of design domain Ω_0 and contacting object Ω'_0. (b) Main computational steps in the hybrid MPM framework, consisting of the F2C, C2G, G2C, and C2F mapping operations. (c) Schematic of the mappings between the Eulerian grid and the CPs.

F2C step. A key feature of the hybrid MPM is the introduction of CPs along the surface of the continuum represented by FE nodes. As an example, Fig. 1(b) illustrates the configuration for a two-dimensional analysis. In this case, the continuum surface is a one-dimensional curve, and two CPs are placed at equal spacing between every pair of adjacent FE nodes. It should be noted that the number of CPs is dictated by the resolution required to accurately resolve the contact boundary, which naturally scales with the spatial dimensionality of the problem.

Let $\boldsymbol{x}_q$ denote the coordinates of a CP located on the surface. The mass m_q and velocity $\boldsymbol{v}_q$ of the CP are interpolated from those of the neighboring FE nodes α as follows:

$$m_q = \sum_\alpha B_\alpha(\boldsymbol{x}_q)\, m_\alpha, \quad \boldsymbol{v}_q^* = \sum_\alpha B_\alpha(\boldsymbol{x}_q)\, \boldsymbol{v}_\alpha^*. \tag{4}$$

Here, $B_\alpha := K_\alpha|_\Gamma$ denotes the trace of the shape function K_α on the boundary Γ. It should be emphasized that, when computing the mass m_q and velocity $\boldsymbol{v}_q^*$ of the CPs, only the FE nodes lying on the surface are used; contributions from interior FE nodes are excluded from the interpolation. This is physically consistent, as contact interactions in continuum mechanics act exclusively through the surfaces of the bodies.

C2G step. In the second step of the analysis, the mass, momentum, and velocity of the CPs are mapped to the neighboring Eulerian grid. Let $\boldsymbol{x}_i$ denote the position of an Eulerian grid, and let $\boldsymbol{d}_{iq} = \boldsymbol{x}_q - \boldsymbol{x}_i$ be the relative position vector between the grid and the CP. The velocity $\boldsymbol{v}_i^*$ at the Eulerian grid is computed from the surrounding CP velocities $\boldsymbol{v}_q^*$ as follows:

$$\boldsymbol{v}_i^* = \frac{\sum_{q\in Q_i} \psi(\boldsymbol{d}_{iq})\, m_q \boldsymbol{v}_q^*}{\sum_{q\in Q_i} \psi(\boldsymbol{d}_{iq})\, m_q}. \tag{5}$$

Here, the denominator represents the mapped mass m_i, whereas the numerator corresponds to the mapped momentum $(m\boldsymbol{v}^*)_i$. The Eulerian-grid velocity $\boldsymbol{v}_i^*$ is thus obtained by taking the ratio of these two quantities. Here, the kernel function ψ decreases monotonically with the distance $|\boldsymbol{d}_{iq}|$, and the mapping therefore corresponds to a distance-dependent weighted average: quantities carried by nearby CPs contribute predominantly to the Eulerian grid, whereas those from distant CPs have only a minor influence. In the present study, we employ the second-order B-spline as the kernel function ψ, whose support spans three grid spacings in each coordinate direction (see Fig. 1(c)). The summations in Eq. (5) are taken over the set of CPs within its support around the Eulerian grid i, $Q_i := \{\, q \mid |d_{iq,k}| \le 3\Delta x/2,\ k \in \{x, y, z\} \,\}$, where $d_{iq,k}$ and Δx denote the kth component of $\boldsymbol{d}_{iq}$ and the Eulerian grid spacing, respectively.

G2C and C2F steps. The remaining two steps are essentially the reverse of the previous ones. The velocity of Eulerian grid $\boldsymbol{v}_i^*$ can be mapped back to CPs using the same kernel function ψ such that

$$\boldsymbol{v}_q^{**} = \sum_i \psi(\boldsymbol{d}_{iq})\boldsymbol{v}_i^*. \tag{6}$$

Here, we define the velocity difference before and after the round-trip mapping between the CPs and the Eulerian grid as $\Delta \boldsymbol{v}_q = \boldsymbol{v}_q^{**} - \boldsymbol{v}_q^{*}$. Unfortunately, this velocity difference $\Delta \boldsymbol{v}_q$ may induce non-physical numerical adhesive forces between the bodies. To avoid this issue, we replace $\Delta \boldsymbol{v}_q$ with a modified velocity difference $\Delta \boldsymbol{v}'_q$ (see Eq. (12)). Although the details are provided in the next section, the corrected velocity difference $\Delta \boldsymbol{v}'_q$ fully eliminates this problem. The updated velocities are then mapped back from the CPs to the FE nodes using the interpolation function B_α:

$$\Delta \boldsymbol{v}'_\alpha = \frac{\sum_q B_\alpha(\boldsymbol{x}_q) m_q \Delta \boldsymbol{v}'_q}{\sum_q B_\alpha(\boldsymbol{x}_q) m_q}. \tag{7}$$

Similar to Eq. (5), the denominator and numerator correspond to the mapped mass m_α and mapped momentum $(m\boldsymbol{v}')_\alpha$ of the FE node α, respectively.

Finally, the updated velocity and configuration of FE node at the $(n+1)$-th step is expressed as

$$\boldsymbol{v}_\alpha^{(n+1)} = \begin{cases} \boldsymbol{v}_\alpha^{*} & (\text{in} \quad \Omega_0) \\ \boldsymbol{v}_\alpha^{*} + \Delta \boldsymbol{v}'_\alpha & (\text{on} \quad \Gamma_N), \end{cases} \qquad \boldsymbol{x}_\alpha^{(n+1)} = \boldsymbol{x}_\alpha^{(n)} + \Delta t \boldsymbol{v}_\alpha^{(n+1)}. \tag{8}$$

As explained previously, $\boldsymbol{v}_\alpha^{*}$ denotes the tentative velocity obtained from the explicit FEM formulation. Compared with Eq. (3), nothing changes in the interior of the domain; modifications occur only at the boundaries through the velocity correction $\Delta \boldsymbol{v}'_\alpha$. It is important to note that no surface tracking is required, because the correction $\Delta \boldsymbol{v}'_\alpha$ is automatically applied at every time step during the numerical integration of the equations of motion. This constitutes the computational scheme in the hybrid MPM.

2.3. Directional velocity averaging and friction

In contact analysis using the hybrid MPM, the velocity change on a CP, namely $\Delta \boldsymbol{v}_q$ defined as the difference between Eqs. (4) and (6), contains the essential information regarding the contact interactions between deformable bodies:

$$\Delta \boldsymbol{v}_q = \boldsymbol{v}_q^{**} - \boldsymbol{v}_q^{*}. \tag{9}$$

However, this quantity cannot be directly employed in the MPM simulations because it leads to non-physical numerical adhesion. To address this issue, a necessary modification was proposed by Bardenhagen et al. [47] and Huang et al. [54]. Below, we briefly review this problem and associated modification scheme. We also provide a brief explanation of how Coulomb friction is incorporated at the contact interface.

As shown in Fig. 2(a), consider the case in which a body Ω_0 approaches the contacting object Ω'_0 with the CP velocity $\boldsymbol{v}_q^{*}$. After applying the C2G and G2C mapping steps, the two bodies acquire velocities in the same direction, which automatically prevents non-physical interpenetration during dynamic contact. In other words, the collision of Ω_0 against Ω'_0 is correctly captured. In contrast, Fig. 2(b) depicts a configuration in which Ω_0 moves away from Ω'_0. If the same two mapping steps (C2G and G2C) are applied, both bodies again begin to move in the same direction; that is, Ω'_0 starts to follow the motion of Ω_0. This behavior constitutes a non-physical numerical adhesion that should not arise in reality and can significantly deteriorate the accuracy of MPM simulations. To overcome this issue, we modify the $\Delta \boldsymbol{v}_q$, defined in Eq. (9), based on the relative direction of motion. More specifically, we evaluate the relative motion using the inner product $\Delta \boldsymbol{v}_q \cdot \boldsymbol{n}_q$, where $\boldsymbol{n}_q$ denotes the outward unit normal vector on the contact boundary Γ_C at the CP, as shown in Fig. 2. When the bodies approach each other ($\Delta \boldsymbol{v}_q \cdot \boldsymbol{n}_q < 0$), the original $\Delta \boldsymbol{v}_q$ is retained to represent collision effects. Conversely, when the bodies separate ($\Delta \boldsymbol{v}_q \cdot \boldsymbol{n}_q > 0$), the non-physical adhesive contribution is removed by setting the velocity correction to zero. Mathematically, the correction of $\Delta \boldsymbol{v}_q$ based on the relative orientation can be cast into the following elastic impulse function.

$$I_q = \begin{cases} (1+e) m_q \Delta \boldsymbol{v}_q \cdot \boldsymbol{n}_q & (\Delta \boldsymbol{v}_q \cdot \boldsymbol{n}_q < 0) \\ 0 & (\Delta \boldsymbol{v}_q \cdot \boldsymbol{n}_q > 0) \end{cases}. \tag{10}$$

Here, e denotes the coefficient of restitution. For simplicity, we set $e = 1$, representing a perfectly elastic collision, throughout this study. This formulation implies that an elastic impulse arises exclusively when the contact interfaces are sufficiently proximal to trigger the velocity difference $\Delta \boldsymbol{v}_q$, provided that the interfaces are in an approach phase, i.e., $\Delta \boldsymbol{v}_q \cdot \boldsymbol{n}_q < 0$. The elastic impulse in Eq. (10) is discontinuous by definition at $\Delta \boldsymbol{v}_q \cdot \boldsymbol{n}_q = 0$, which precludes its direct use in sensitivity analysis for gradient-based TO. To overcome this difficulty, the present study introduces the following regularized expression:

$$I'_q = m_q \Delta \boldsymbol{v}_q \cdot \boldsymbol{n}_q \left(-\tanh(\beta_n \Delta \boldsymbol{v}_q \cdot \boldsymbol{n}_q) + 1 \right). \tag{11}$$

Here, β_n is a steepness parameter that controls the sharpness of the transition. With this continuous switching function, in the limit $\Delta \boldsymbol{v}_q \cdot \boldsymbol{n}_q \to -\infty$ we obtain $I'_q \to 2 m_q \Delta \boldsymbol{v}_q \cdot \boldsymbol{n}_q$, which corresponds to a perfectly elastic collision. Conversely, as $\Delta \boldsymbol{v}_q \cdot \boldsymbol{n}_q \to +\infty$, $I'_q \to 0$, and the contact force is fully deactivated during separation. Using the continuous elastic response function I'_q given in Eq. (11), we finally end up with the correct velocity difference $\Delta \boldsymbol{v}'_q$ such that

$$\Delta \boldsymbol{v}'_q = \Delta \boldsymbol{v}'_{q,\text{norm}} + \Delta \boldsymbol{v}'_{q,\tan}, \tag{12}$$

where $\Delta \boldsymbol{v}'_{q,\text{norm}} = (I'_q / m_q) \boldsymbol{n}_q$ denotes the velocity difference in the normal direction. The other term $\Delta \boldsymbol{v}'_{q,\tan}$ describes the change in the tangential direction where we need careful consideration.

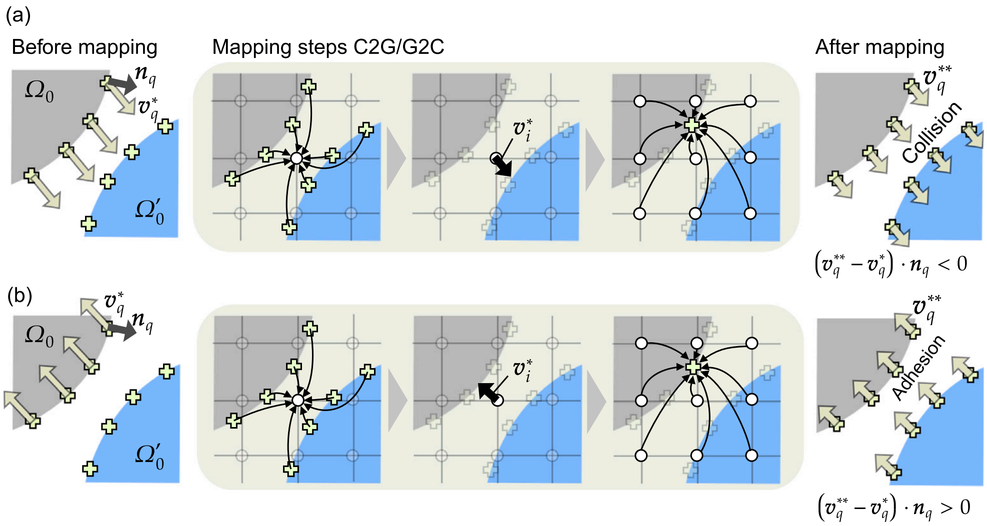

Fig. 2. Schematic illustration of velocity averaging through the C2G and G2C mappings. In the approaching case (a), the mappings prevent non-physical interpenetration. In the separating case (b), the same averaging produces non-physical numerical adhesion.

As explained in Fig. 2(a), the forward C2G/G2C mapping averages the normal velocity of the contacting surfaces so that the non-penetration condition is satisfied. A similar correction is applied to the tangential velocity: the interface enters a no-slip, or stick, state when the tangential velocity changes become identical through the mapping. In this study, we employ a more general frictional contact model by introducing an additional slip state [45]. To this end, we consider two possible states of the contact interface—stick and slip—and define the corresponding velocities as follows:

$$V_{\text{stick}} = \left|\boldsymbol{\Delta v}_{q,\tan}\right|, \qquad V_{\text{slip}} = -\mu_f \boldsymbol{\Delta v}'_{q,\text{norm}} \cdot \boldsymbol{n}_q, \tag{13}$$

where V_{stick} represents the stick velocity, defined using the tangential component of the velocity change $\boldsymbol{\Delta v}_{q,\tan} = \boldsymbol{\Delta v}_q - (\boldsymbol{\Delta v}_q \cdot \boldsymbol{n}_q)\boldsymbol{n}_q$. In contrast, V_{slip} denotes the slip velocity, which depends on the normal component and the friction coefficient μ_f. The actual tangential velocity change is taken as the smaller of the two values, thereby implementing Coulomb friction. The explicit formula is written as follows:

$$\boldsymbol{\Delta v}'_{q,\tan} = \min\left(V_{\text{stick}}, V_{\text{slip}}\right) \frac{\boldsymbol{\Delta v}_{q,\tan}}{\left|\boldsymbol{\Delta v}_{q,\tan}\right|}. \tag{14}$$

Unfortunately, Eq. (14) is not differentiable at the stick–slip transition $V_{\text{stick}} = V_{\text{slip}}$, and is therefore unsuitable for sensitivity analysis. To address this issue, we employ a square-root regularization [36,55]:

$$\boldsymbol{\Delta v}'_{q,\tan} = \frac{V_{\text{slip}}}{\sqrt{V_{\text{stick}}^2 + V_{\text{slip}}^2 + \epsilon_{\tan}}} \boldsymbol{\Delta v}_{q,\tan}. \tag{15}$$

Here, $\epsilon_{\tan}$ is a small constant introduced to avoid division by zero when $V_{\text{stick}} = V_{\text{slip}} = 0$. It is noted that previous studies applied smoothing to the tangential force, whereas in the present work the smoothening is applied to the tangential velocity.

3. Topology optimization for dynamic problems involving mechanical contact and friction

3.1. Mathematical formulation of the optimization problem

One of the major challenges in modern topology optimization is the treatment of dynamic problems involving mechanical contact. Although FEM-based computational schemes for dynamic TO have been extensively developed [19,56], the treatment of contact interactions in such frameworks generally requires explicit contact detection and can therefore impose a considerable computational burden. As demonstrated in the previous section, dynamic analyses by the hybrid MPM are essentially equivalent to those conducted with FEM. This relationship arises from the fact that the hybrid MPM formulation is obtained by simply replacing the velocity update in Eq. (3) with the expression given in Eq. (8). This correspondence in mathematical structure allows conventional FEM-based TO frameworks to be transferred directly to the hybrid MPM setting, thereby enabling a systematic extension of the dynamic TO formulations to problems involving mechanical contact and friction. Alternative approaches based on the standard MPM have also been proposed for TO [40–44]. However, the particle-based standard MPM inevitably suffers from accuracy degradation due to repeated stress updates, whereas the hybrid MPM maintains accuracy by computing internal forces within a total Lagrangian framework [46]. Moreover, the hybrid MPM helps prevent unintended failure [57,58] and is expected to provide stable numerical performance even under large deformations, including applications to highly compliant structures such as soft robots.

Following previous studies on dynamic TO using FEM [19,56], we generalize the formulation to problems involving mechanical contact. For simplicity, we introduce a state vector that collects all nodal velocities and coordinates at the nth time step, denoted by $\boldsymbol{y}^{(n)} := ([\boldsymbol{v}_\alpha^{(n)}]_{\alpha\in\mathcal{N}_{\mathrm{FA}}}, [\boldsymbol{x}_\alpha^{(n)}]_{\alpha\in\mathcal{N}_{\mathrm{FA}}})$, where $\mathcal{N}_{\mathrm{FA}}$ denotes the set of all FE nodes. The optimization problem can then be written in the following abstract form:

$$\min_{\theta} \quad F\left(\theta, \boldsymbol{y}^{(0)}, \dots, \boldsymbol{y}^{(N_T)}\right) = \frac{1}{N_T}\sum_{n=0}^{N_T} f^{(n)}\left(\theta, \boldsymbol{y}^{(n)}\right), \tag{16}$$

$$\text{subject to} \quad \boldsymbol{y}^{(n+1)} - \boldsymbol{\mathcal{T}}\left(\theta, \boldsymbol{y}^{(n)}\right) = 0 \qquad (n \in \{0, \dots, N_T - 1\}), \tag{17}$$

together with the inequality constraints

$$\int_{\Omega_{\mathrm{ds}}} \tilde{\theta} dV \le \alpha_V \int_{\Omega_{\mathrm{ds}}} dV, \quad 0 \le \theta \le 1. \tag{18}$$

Eq. (16) specifies the minimization of the objective function F, which is defined as the time-average of an arbitrary function $f^{(n)} = f(\theta, \boldsymbol{y}^{(n)})$ expressed in terms of the design variable $\theta = \theta(\boldsymbol{X}) \in [0, 1]$ and the entire motion history of the deformable body $\boldsymbol{y}^{(n)}$ $(n \in [0, \dots, N_T])$. The subsidiary condition is given in Eq. (17), where $\boldsymbol{\mathcal{T}}$ denotes the time-integration operator that advances all nodal velocities and coordinates from the nth to the $(n+1)$th time step, as described by Eq. (8) rather than by Eq. (3). By modifying only the construction of $\boldsymbol{\mathcal{T}}$ while retaining the remainder of the existing framework, contact analysis can thus be incorporated naturally within the TO. From the standpoint of computational mechanics, this condition represents the residual of the equations of motion governing the deformable-body contact dynamics.

Eq. (18) represents the inequality constraints associated with the optimization problem. Specifically, the first equation imposes a volume constraint, where α_V denotes the prescribed admissible volume fraction, and the second specifies the admissible range of the design variable θ. $\Omega_{\mathrm{ds}} \subset \Omega_0$ denotes the actual design subdomain, excluding certain problem-dependent non-design regions Ω_{nds} (see details in the next section). $\tilde{\theta}$ in Eq. (18) denotes the filtered design variable, which is a spatially smoothed field of the original design variable θ, introduced to suppress numerical instabilities such as checkerboarding. The filtering procedure is described in Appendix A, while the interpolation schemes for the material parameters and the strain energy density are summarized in Appendix B.

3.2. Sensitivity analysis

For notational simplicity, the time history of the state vector is hereafter collectively denoted by $\boldsymbol{Y} := (\boldsymbol{y}^{(0)}, \dots, \boldsymbol{y}^{(N_T)})$, and the objective function and the time-integration operator at a specific time step n are written as $f^{(n)} = f(\theta, \boldsymbol{y}^{(n)})$ and $\boldsymbol{\mathcal{T}}^{(n)} = \boldsymbol{\mathcal{T}}(\theta, \boldsymbol{y}^{(n)})$, respectively. In addition, the adjoint variable associated with the subsidiary condition Eq. (17) is denoted by $\lambda^{(n)}$, and its collection by $\boldsymbol{\Lambda} = (\lambda^{(1)}, \dots, \lambda^{(N_T)})$. To compute the sensitivity of the optimization problem, we employ the adjoint-variable method and formulate the minimization of the Lagrangian $\mathcal{L}$ such that

$$\min_{\theta} \quad \mathcal{L}(\theta, \boldsymbol{Y}, \boldsymbol{\Lambda}) = \frac{1}{N_T}\sum_{n=0}^{N_T} f^{(n)} + \sum_{n=0}^{N_T-1} \lambda^{(n+1)} \cdot \left(\boldsymbol{y}^{(n+1)} - \boldsymbol{\mathcal{T}}^{(n)}\right). \tag{19}$$

At the minimized state, the Gâteaux derivative of the Lagrangian $\mathcal{L}$ must vanish. Following the derivation procedure in Ref. [59], the governing equations for $\boldsymbol{Y}$ and $\boldsymbol{\Lambda}$, as well as the expression for the sensitivity $\partial\mathcal{L}/\partial\theta$, are derived as follows:

$$\boldsymbol{y}^{(n+1)} = \boldsymbol{\mathcal{T}}^{(n)} \quad \left(n \in \left\{0, \dots, N_T - 1\right\}\right), \tag{20}$$

$$\lambda^{(n)} = -\frac{1}{N_T}\frac{\partial f^{(n)}}{\partial \boldsymbol{y}^{(n)}} + \frac{\partial\left(\lambda^{(n+1)} \cdot \boldsymbol{\mathcal{T}}^{(n)}\right)}{\partial \boldsymbol{y}^{(n)}} \quad \left(n \in \left\{1, \dots, N_T - 1\right\}\right), \quad \lambda^{(N_T)} = -\frac{1}{N_T}\frac{\partial f^{(N_T)}}{\partial \boldsymbol{y}^{(N_T)}}, \tag{21}$$

$$\frac{\partial \mathcal{L}}{\partial \theta} = \sum_{n=0}^{N_T} \frac{1}{N_T}\frac{\partial f^{(n)}}{\partial \theta} - \sum_{n=0}^{N_T-1} \frac{\partial\left(\lambda^{(n+1)} \cdot \boldsymbol{\mathcal{T}}^{(n)}\right)}{\partial \theta}. \tag{22}$$

Eq. (20) recovers the subsidiary condition given in Eq. (17). According to Eq. (21), the adjoint variables $\boldsymbol{\Lambda}$ can be explicitly evaluated in a backward manner, $\lambda^{(n+1)} \to \lambda^{(n)}$, after the state vectors $\boldsymbol{Y}$ have been determined from Eq. (20). Then, substituting both $\boldsymbol{Y}$ and $\boldsymbol{\Lambda}$ into Eq. (22) yields the sensitivity. In this process, we require the derivative of the inner product $\lambda^{(n+1)} \cdot \boldsymbol{\mathcal{T}}^{(n)}$ with respect to the design variable θ. Unfortunately, an analytical expression cannot be obtained because the time integration operator $\mathcal{T}^{(n)}$ involves the complex MPM mapping process. Therefore, we employed the automatic differentiation functionality provided in Taichi [60,61], which computes partial derivatives of a global scalar function with respect to fields stored at FE nodes. This concludes the derivation of the equations used for the sensitivity analysis.

3.3. Optimization flow

The computational flow of the TO procedure is summarized in Algorithm 1. First, we set up the dynamic structural analysis following the standard FEM procedure, that is, by defining the geometry and boundary conditions and prescribing the motion of the contacting body. Then, we define the objective functional for the associated optimization problem. The design variable θ is initially set to 0.5 throughout the design domain Ω_{ds}, whereas it is fixed at $\theta = 1$ in the non-design region Ω_{nds}. The optimization loop consists of adjoint-based sensitivity analysis, design-variable update, and convergence check, as outlined in Section 3.2. The procedure is summarized as follows:

1. **Structural analysis:** The velocity and coordinate at each node, $\boldsymbol{v}_\alpha$ and $\boldsymbol{x}_\alpha$, are first reset to their initial values, $\boldsymbol{v}_\alpha^{(0)}$ and $\boldsymbol{x}_\alpha^{(0)}$. Using these as the starting state, the nodal values at all subsequent time steps, $\boldsymbol{v}_\alpha^{(n)}$ and $\boldsymbol{x}_\alpha^{(n)}$ ($n \in 0, \dots, N_T$), are computed in ascending order through a forward structural analysis. The update of velocities and coordinates at each time step follows the time-integration scheme for dynamic frictional contact described in Section 2. The solution at each time step, $\boldsymbol{v}_\alpha^{(n)}$ and $\boldsymbol{x}_\alpha^{(n)}$, is stored as the state vector $\boldsymbol{y}^{(n)} = ([\boldsymbol{v}_\alpha^{(n)}]_{\alpha\in\mathcal{N}_{\text{FA}}}, [\boldsymbol{x}_\alpha^{(n)}]_{\alpha\in\mathcal{N}_{\text{FA}}})$ for use in the subsequent adjoint analysis.
2. **Adjoint analysis:** The adjoint variable at the final time step, $\lambda^{(N_T)}$, is first computed from the terminal condition given by the second relation in Eq. (21). Then, using the state variables $\boldsymbol{y}^{(n)}$ in all time steps, the adjoint variables $\lambda^{(n)}$ are computed in descending order by the first relation (21).
3. **Sensitivity analysis:** Given the time history of the state variable $\boldsymbol{Y}$ and adjoint variables $\boldsymbol{\Lambda}$, the sensitivity $\partial\mathcal{L}/\partial\theta$ is evaluated from Eq. (22).
4. **Design-variable update:** The design variable θ is updated based on the sensitivity field using the Method of Moving Asymptotes (MMA) [62]. In this process, the inequality constraint in Eq. (18) is taken into account. For the implementation, we employ the Python module GCMMA–MMA–Python (mmapy) [63].
5. **Convergence check:** Convergence is checked according to

$$\frac{\left|F_{\text{norm}}^{k+1} - F_{\text{norm}}^{k}\right|}{\max\left(1, \left|F_{\text{norm}}^{k}\right|\right)} < \epsilon_{\text{tol}}, \tag{23}$$

where k denotes the iteration index and ϵ_{tol} is the tolerance. Here, $F_{\text{norm}} = F/|F_0|$ denotes the normalized objective, and F_0 is the objective value at the initial design. Convergence is declared when this condition is satisfied for three consecutive iterations. Once convergence is achieved, the optimization loop is terminated, and the material distribution given by the design variable at iteration k is adopted as the optimal structure.

The parameters commonly used in all analyses are summarized in Table 1, and unless otherwise specified, these values are adopted. The problem-specific parameters are also summarized in Table 2. Computational details, including the hardware and software environment used in the present study and the run time cost of the simulations, are given in Appendix C.

4. Numerical examples

4.1. Compliance minimization with frictional contact: 2D case

This section explores the application of TO to structural problems involving dynamic mechanical contact with interfacial friction. As a first illustrative example, we consider the compliance minimization of a three-point bending configuration, a classical benchmark test in TO. The problem setup is shown in Fig. 3(a), incorporating two critical modifications to the conventional approach. The first concerns the dynamic behavior of the contact interface. In conventional compliance minimization, both the indenter and the supports are often treated as fully fixed Dirichlet boundaries, which is reasonable only when infinitesimally small deformations are considered. However, soft robots typically consist of flexible components and are characterized by large deformations. In the optimal design of such compliant systems and devices, the pronounced deformation of both the design domain and the supports leads to a dynamic shift in the contact location. As the first generalization, we therefore perform TO under evolving contact locations by allowing the indenter to move not only vertically but also laterally. The second generalization follows naturally from the first: the lateral motion of the indenter necessarily induces interfacial friction, a factor rarely considered in previous TO studies. Here, we examine how the inclusion of Coulomb friction alters the resulting optimal structure by incorporating the friction model into the tangential motion.

To simultaneously control the vertical and lateral motions of the indenter, we prescribe the Dirichlet boundary Γ_D^u at the top end of the indenter, as shown in Fig. 3(a) and (b), whereas the bottom supports remain fixed. More specifically, the displacements $\bar{\boldsymbol{u}}$ prescribed on the boundary are given as follows:

$$\bar{\boldsymbol{u}} = \left(\bar{u}_x\left(1 - \cos\frac{\pi\phi(t)}{2}\right), -\bar{u}_z\phi(t)\right), \quad \text{with} \quad \phi(t) = \begin{cases} \dfrac{t^2}{t_1(2T - t_1)}, & 0 \le t \le t_1 \\ \dfrac{2t - t_1}{2T - t_1}, & t_1 \le t \le T \end{cases}, \tag{24}$$

where $\bar{u}_x$ and $\bar{u}_z$ denote the lateral and vertical displacements, respectively, throughout the motion, and t_1 denotes the end time of the initial ramping phase of the prescribed motion, and we set $t_1 = 0.4T$. The non-design regions Ω_{nds} are introduced to enhance

Algorithm 1: Optimization flow

```
% Problem formulation of TO, including dynamic contact and friction of deformable bodies.
Formulate the structural analysis following the standard FEM procedure.
Define the objective function in Eq (16).
Initialize the design-variable field in design domain with a uniform value of 0.5.
while True do
    k ← k + 1 (k denotes iteration step)
    % Dynamical structure analysis with friction contact using Hybrid MPM.
    Reset the velocity and coordinate fields to the initial conditions.
    for Incremental time step n = 0 to N_T − 1 do
        % Update velocity and coordinate fields according to the flow in Subsection 2.2.
        Update the velocity field at FE nodes according to Eq. (3).
        F2C step : map physical quantities from the FE nodes to the CPs according to Eq. (4)
        C2G steps : map physical quantities from the CPs to the Eulerian grids according to Eq. (5)
        G2C steps : interpolate the velocity at the CPs from Eulerian grids according to Eq. (6)
        Compute the contact-corrected velocity at the CPs due to frictional contact.
        C2F : map the contact-corrected velocity from the CPs back to the FE nodes using Eq. (7).
    % Adjoint analysis
    Compute the adjoint variables at n = N_T according to second relation Eq. (21)
    for Backward step time n = N_T − 1 down to 1 do
        Update the adjoint variables according to first relation Eq. (21).
    % Sensitivity analysis
    Compute the sensitivity field according to Eq. (22).
    % Design variable update
    Update design variable field using MMA [62].
    if The convergence criterion in Eq. (23) is satisfied for three consecutive iterations then
        exit
```

Table 1
The parameters commonly used in the topological optimization with mechanical contacts.

Symbol	Description	Unit	Value	
Material parameters				
			Material 1	Material 2
ρ_0	Mass density	kg/mm^3	1.0×10^{-6}	5.0×10^{-6}
E_0	Young's modulus	MPa	1	25
ν	Poisson's ratio	–	0.3	0.2
Parameters for structure analysis				
$\boldsymbol{b}_0$	Local body-force density vector in Eq. (2)	N/mm^3	$\boldsymbol{0}$	
$\bar{\boldsymbol{t}}_0$	Local traction vector in Eq. (2)	MPa	$\boldsymbol{0}$	
β_n	Steepness parameter in Eq. (11)	–	200	
$\epsilon_{\tan}$	Stabilization parameter in Eq. (15)	–	1.0×10^{-6}	
Parameters for TO				
p	SIMP penalization exponent in Eq. (B.5)	–	3	
$\gamma_{\min}$	Minimum Young's modulus ratio in Eq. (B.5)	–	1.0×10^{-4}	
α_V	Volume fraction in Eq. (18)	–	0.4 (2D analysis)	
		–	0.2 (3D analysis)	
β_φ	Steepness parameter in Eq. (B.7)	–	500	
ω_φ	Threshold parameter in Eq. (B.7)	–	0.03	

the numerical stability. The material parameters for all deformable bodies, including the contacting bodies Ω_0', are assigned the properties of Material 1 listed in Table 1.

We formulate the compliance minimization problem by maximizing the work done by the prescribed motion of the indenter. Let $\boldsymbol{\tau}^{(n)}$ denote the surface traction on Γ_D^u generated by the motion given in Eq. (24). The work done by the indenter on the design domain is defined as the boundary integral of the inner product $\boldsymbol{\tau}^{(n)} \cdot \bar{\boldsymbol{u}}^{(n)}$. After FE discretization, the external work function at the nth step is expressed as

$$f_S^{(n)} = -\int_{\Gamma_D^u} \boldsymbol{\tau}^{(n)} \cdot \bar{\boldsymbol{u}}^{(n)} d\Gamma = \sum_{\alpha \in \mathcal{N}_{\mathrm{FU}}} \left\{ \boldsymbol{f}_\alpha^{\mathrm{int}(n)} - \frac{m_\alpha}{\Delta t} \left(\bar{\boldsymbol{v}}_\alpha^{(n+1)} - \bar{\boldsymbol{v}}_\alpha^{(n)} \right) \right\} \cdot \bar{\boldsymbol{u}}_\alpha^{(n)}, \tag{25}$$

where $\mathcal{N}_{\mathrm{FU}}$ denotes the set of FE nodes on the boundary Γ_D^u, and $\bar{\boldsymbol{v}}_\alpha^{(n)} = d(\bar{\boldsymbol{u}}_\alpha^{(n)})/dt$ is the corresponding velocity. The term in parentheses on the right-hand side represents the reaction forces associated with the surface traction $\boldsymbol{\tau}^{(n)}$, indicating that they must

Table 2
Problem-specific numerical parameters for all examples.

Symbol	Description	Unit	Compl. min., 2D	Compl. min., 3D	Brake, 2D	Brake, 3D
ϵ_{tol}	Convergence tolerance in Eq. (23)	–	1.0×10^{-5}	1.0×10^{-5}	2.0×10^{-5}	1.0×10^{-5}
Δt	Time step size	s	2.5×10^{-6}	5.0×10^{-6}	2.5×10^{-6}	5.0×10^{-6}
N_T	Total number of time steps	–	6000	3000	6000	2000
–	Number of CPs per boundary facet	–	4	9(=3 × 3)	4	9(=3 × 3)
–	Finite element size	mm	1	2	0.8	2
–	Spacing of Eulerian grid nodes	mm	0.5	1	0.4	1
–	Eulerian grid range in x-direction	mm	[−100, 100]	[−80, 80]	[−150,150]	[−75, 75]
–	Eulerian grid range in y-direction	mm	–	[−80, 80]	–	[−30, 30]
–	Eulerian grid range in z-direction	mm	[−100, 100]	[−50, 100]	[−100, 200]	[−50, 100]

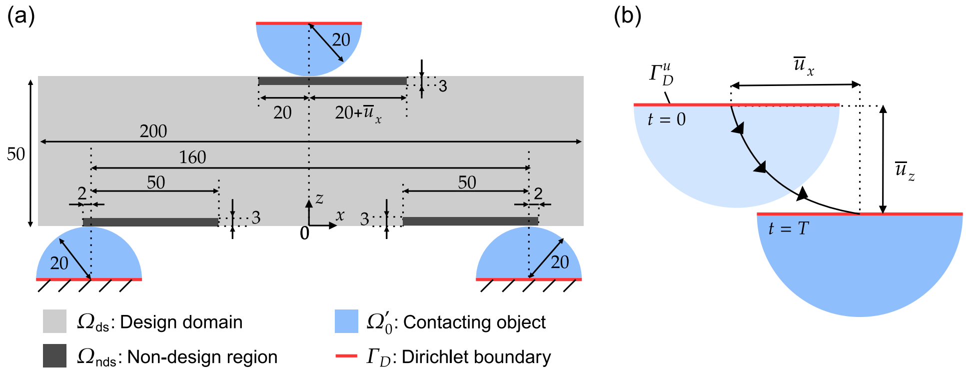

Fig. 3. (a) Simulation setup for the compliance minimization problem in three-point bending with dynamic contact and friction. All dimensions are given in millimeters [mm]. (b) Schematic illustration of the prescribed displacement trajectory of the indenter.

balance the internal forces and inertial forces arising from the prescribed motion of the indenter. Eq. (25) therefore defines the objective function at the nth step. Inserting $f_S^{(n)}$ into the right-hand side of Eq. (16) yields the objective function $F(\theta, \boldsymbol{Y})$ to be minimized, thereby completing the formulation of the compliance minimization problem. This expression is also directly applicable to the sensitivity analysis.

We consider TO under six dynamic indentation conditions, combining three lateral displacements ($\bar{u}_x$ = 0, 7.5, and 15 mm) with two friction coefficients (μ_f = 0 and 0.25). In all cases, the maximum vertical displacement is fixed at $\bar{u}_z$ = 10 mm. Fig. 4 summarizes the resulting optimal structures and their corresponding deformed configurations. Fig. 4(a), (b), and (c) show the cases without interfacial friction ($\mu_f = 0$). As seen in (a), purely vertical loading yields an optimal structure that remains perfectly symmetric with respect to the z-axis, and this overall structural feature is consistent with those reported in previous studies under similar boundary and loading conditions [30,64,65]. However, this symmetry is lost once lateral displacement is applied. As the prescribed lateral displacement increases, the material distribution θ progressively shifts toward the right to effectively accommodate the induced momentum. In particular, the member extending from the upper center toward the right support becomes noticeably thicker, reflecting the increased structural demand to resist the additional lateral loading. These observations collectively indicate that lateral motion significantly alters both the topology and the geometry of the optimal structure. The color map in the deformed configurations presents the strain energy density φ at the final simulation step N_T. Consistent with the shifted material distribution, strain energy localizes more intensely near the right support. High concentrations also appear near the contact regions of the indenter and the supports, where deformation is most pronounced. The effects of interfacial friction on the optimal structures are summarized in Fig. 4(d), (e), and (f). Although the overall distribution of θ appears broadly consistent with their non-frictional counterparts, the resulting topologies generally exhibit increased complexity. Specifically, the influence of friction becomes most pronounced directly beneath the indentation point, while it remains negligible near the supports at the bottom of the design domain, even though friction is uniformly considered across all contact interfaces. This pronounced structural change induced by friction is a noteworthy and somewhat unexpected finding.

Fig. 5 shows the time evolution of the external work $f_S^{(n)}$, defined in Eq. (25), obtained from the optimized structures. In all six cases, the external work f_S increases with time. For case (a), where $\bar{u}_x$ = 0 mm, interfacial friction has no influence on the time history of the external work. This is expected, as friction contributes solely to the tangential component, as indicated in Eq. (14). In contrast, for cases (b) ($\bar{u}_x$ = 7.5 mm) and (c) ($\bar{u}_x$ = 15 mm), the presence of friction yields a clear difference in the time evolution. In both scenarios, the external work grows more rapidly when friction is present. This accelerated behavior is directly attributed to the additional frictional forces generated between the indenter and the design domain.

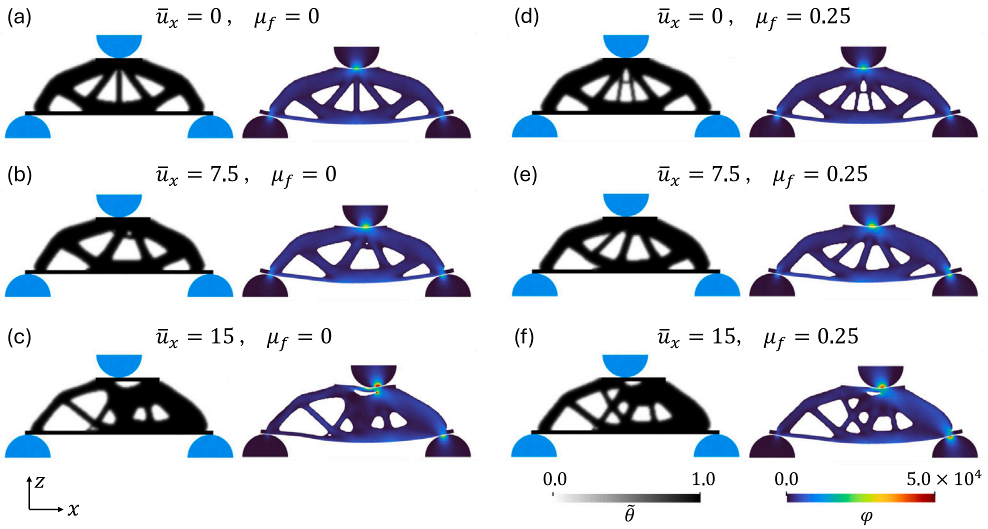

Fig. 4. Optimized structures and strain energy distributions at the deformed configurations for the compliance minimization of the three-point bending problem. Panels (a)–(f) correspond to combinations of three lateral displacements and two friction coefficients: (a) $\bar{u}_x = 0$, (b) $\bar{u}_x = 7.5$, and (c) $\bar{u}_x = 15$ with a friction coefficient of $\mu_f = 0$; (d) $\bar{u}_x = 0$, (e) $\bar{u}_x = 7.5$, and (f) $\bar{u}_x = 15$ with a friction coefficient of $\mu_f = 0.25$. The filtered design variable $\tilde{\theta}$ is used for visualization. (For interpretation of the references to color in this figure legend, the reader is referred to the web version of this article.)

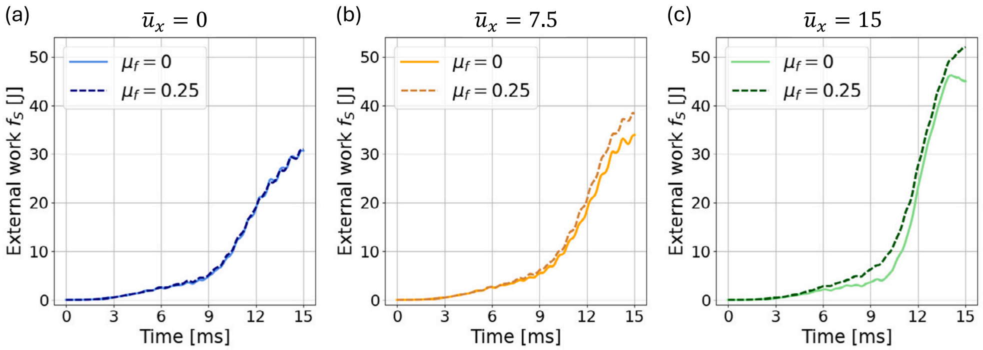

Fig. 5. Time evolution of the external work f_S, defined in Eq. (25), for optimized structures shown in Fig. 4. The results for friction coefficients $\mu_f = 0.0$ (solid curve) and $\mu_f = 0.25$ (dashed curve) are compared for different prescribed horizontal displacements $\bar{u}_x$ of the indenter: (a) $\bar{u}_x = 0$, (b) $\bar{u}_x = 7.5$ mm, and (c) $\bar{u}_x = 15$ mm.

4.2. Compliance minimization with frictional contact: 3D case

We extend the compliance minimization problem presented in the previous section to a general three-dimensional (3D) setting. The configuration and geometric dimensions of the model are shown in Fig. 6(a). The optimization target is a rectangular parallelepiped design domain clamped by a hemispherical indenter and supports of identical radius. The Dirichlet boundary conditions are imposed in the same manner as in the 2D case: the four supports are fully fixed, whereas a prescribed displacement is applied to the indenter (see Fig. 6(b)). The motion of the indenter is given by the following expression:

$$\bar{\boldsymbol{u}} = \left(\bar{u}_x\left(1 - \cos\left(\frac{\pi}{2}\phi(t)\right)\right), \bar{u}_y\left(1 - \cos\left(\frac{\pi}{2}\phi(t)\right)\right), -\bar{u}_z\phi(t)\right), \tag{26}$$

where $\bar{u}_x$, $\bar{u}_y$, and $\bar{u}_z$ are the maximum displacements in each coordinate direction, and $\phi(t)$ denotes the prescribed time evolution given in Eq. (24). Similar to the previous 2D analysis, rectangular non-design regions Ω_{nds} are introduced to enhance the numerical stability. Fig. 6(c) shows the dimensions of the non-design region placed at the top surface of the design domain. The region is defined around the initial contact point with the indenter, $(0, 0, 50)$ at $t = 0$, extending 12 mm in the $\pm x$- and $\pm y$-directions and additionally by $\bar{u}_x$ and $\bar{u}_y$ in the $+x$- and $+y$-directions, respectively, to accommodate the prescribed displacement of the indenter. The optimized structures are investigated under four distinct loading conditions, namely $(\bar{u}_x, \bar{u}_y) = (0, 0)$, $(0, 7.5)$, $(15, 0)$, and $(15, 7.5)$ mm, with a common prescribed vertical displacement of $\bar{u}_z = 10$ mm. In all these cases, the friction coefficient is set to

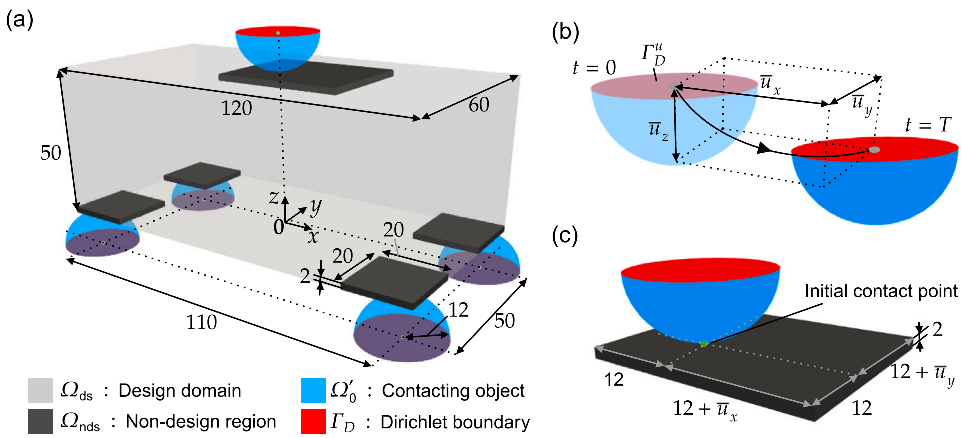

Fig. 6. (a) Simulation setup for the compliance minimization problem in 3D three-point bending with dynamic contact and friction. All dimensions are given in millimeters (mm). (b) Schematic illustration of the prescribed displacement trajectory of the indenter. (c) Dimensions of the rectangular non-design region at the top surface of the design domain Ω_{ds}.

$\mu_f = 0.25$. The material parameters for all deformable bodies, including the contacting bodies Ω'_0, are assigned the properties of Material 1 listed in Table 1.

Fig. 7 presents the optimization results. In case (a), $(\bar{u}_x, \bar{u}_y) = (0, 0)$ mm, where the indenter moves only in the vertical direction, the symmetry of the geometry and boundary conditions yields an optimal structure that is invariant under a 180° rotation about the z-axis. In case (b), $(\bar{u}_x, \bar{u}_y) = (0, 7.5)$ mm, where the indenter moves in the $+y$ and $-z$ directions, the resulting optimal structure is symmetric with respect to the plane $x = 0$. The material distribution θ shifts toward the $+y$ side, forming a continuous, void-free load path along the contact regions between the supports at $y > 0$ and the indenter. In case (c), $(\bar{u}_x, \bar{u}_y) = (15, 0)$ mm, where the motion occurs in the $+x$ and $-z$ directions, the optimal structure becomes symmetric with respect to the plane $y = 0$. Prominent structural members extend toward the supports at $x > 0$ and toward the indenter, effectively supporting the induced lateral loading. Finally, in case (d), $(\bar{u}_x, \bar{u}_y) = (15, 7.5)$ mm, the indenter undergoes an oblique motion in the $+x$, $+y$, and $-z$ directions. The optimal structure detaches from the support located at $(x < 0, y < 0)$, and the principal load paths concentrate through the remaining three supports. These findings are highly consistent with the preceding 2D results and convincingly demonstrate that the proposed mathematical framework for TO under dynamic contact and friction can be naturally and robustly extended to three dimensions.

4.3. An optimal braking structure for a rotating spherical object: 2D case

In the next problem, we directly investigate the effect of interfacial friction within the TO framework, as it is an important mechanical factor in soft robotic gripping, walking, and crawling. Specifically, we consider the design of an optimal braking structure intended to suppress the rotation of a spinning elastic sphere through contact and friction. In this setting, friction plays a central role: as the sphere rotates, tangential contact forces generate a frictional moment that removes angular momentum and gradually brings the sphere to rest. The magnitude and distribution of these frictional forces strongly depend on the evolving contact configuration and the large deformation of both bodies. This problem is particularly challenging because it involves frequent switching of contact interfaces as well as substantial energy dissipation induced by the large deformations of the compliant braking structure. Consequently, it serves as a stringent test of the applicability and robustness of the proposed TO framework.

The experimental setup for the numerical analysis is shown in Fig. 8. A spherical object with radius $R = 10$ mm is spinning counterclockwise with an initial angular velocity of $\omega_{\text{init}} = 1000$ rad/s and collides with the rectangular domain while possessing an initial translational velocity of $v_{\text{init}} = 3000$ mm/s. The rectangular design domain is positioned directly beneath the spinning sphere, and its side edges are mechanically fixed. Both the sphere and the design domain are modeled as elastically deformable bodies. Let us denote the velocity field inside the rotating sphere by $\boldsymbol{v}$. This velocity can be naturally decomposed into two components: $\boldsymbol{v} = \boldsymbol{v}_g + \hat{\boldsymbol{v}}$. Here, $\boldsymbol{v}_g$ represents the center-of-mass (COM) velocity, defined by $\boldsymbol{v}_g = \int_{\Omega_{\text{sph}}} \boldsymbol{v}\, dV / V_{\text{sph}}$, where $V_{\text{sph}} = \int_{\Omega_{\text{sph}}} dV$ denotes the total volume of the sphere in its current configuration. The term $\hat{\boldsymbol{v}}$ represents the relative velocity with respect to the COM, arising from the angular rotation. Similarly, the position vector at each point inside the sphere is decomposed as $\boldsymbol{x} = \boldsymbol{x}_g + \hat{\boldsymbol{x}}$, where $\boldsymbol{x}_g = \int_{\Omega_{\text{sph}}} \boldsymbol{x}\, dV / V_{\text{sph}}$ denotes the volume average position. Let $(\boldsymbol{e}_x, \boldsymbol{e}_y, \boldsymbol{e}_z)$ denote the unit vectors of the Cartesian coordinate system. At the initial time step $n = 0$, the COM velocity and relative velocity are given by $\boldsymbol{v}_g^{(0)} = -v_{\text{init}} \boldsymbol{e}_z$ and $\hat{\boldsymbol{v}}^{(0)} = \hat{\boldsymbol{x}}^{(0)} \times (-\omega_{\text{init}} \boldsymbol{e}_y)$, respectively. We formulate the optimization problem to determine a structure that effectively suppresses the rotational energy of the sphere through frictional contact. To this end, the rotational energy of the sphere is chosen as the objective function, expressed

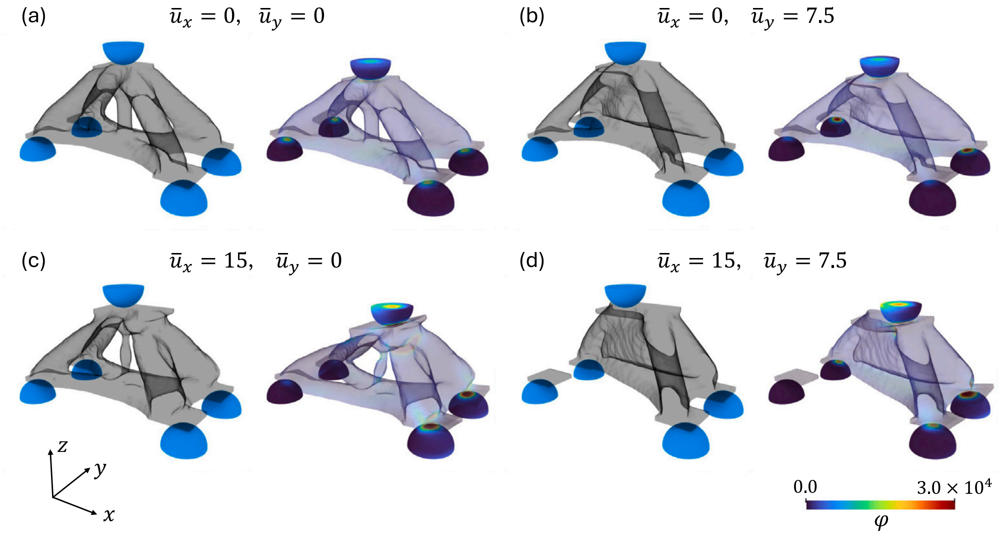

Fig. 7. Optimized structures and strain energy distributions at the deformed configurations for the compliance minimization of the 3D three-point bending problem. (a) $\bar{u}_x = 0$, $\bar{u}_y = 0$; (b) $\bar{u}_x = 0$, $\bar{u}_y = 7.5$; (c) $\bar{u}_x = 15$, $\bar{u}_y = 0$; (d) $\bar{u}_x = 15$, $\bar{u}_y = 7.5$ mm. In each panel, the optimized structure is shown on the left as the region where $\tilde{\theta} \geq 0.5$. The deformed configuration at $t = T$ is shown on the right, colored by the local strain energy density φ. (For interpretation of the references to color in this figure legend, the reader is referred to the web version of this article.)

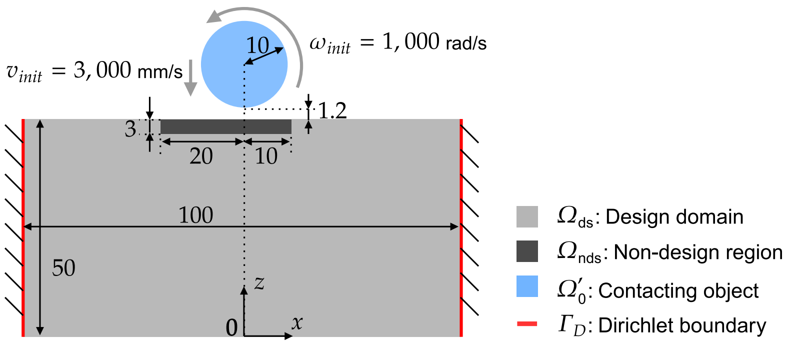

Fig. 8. Simulation setup for the 2D optimal braking structure for a rotating spherical object. The non-design region is introduced to enhance the numerical stability of the TO analysis. All dimensions are given in millimeters (mm).

at the nth time step as

$$f_R^{(n)} = \frac{1}{2} \int_{\Omega_{\text{sph}}} \frac{L_{\text{sph}}^{(n)2}}{I_{\text{sph}}^{(n)}} \, dV, \tag{27}$$

where $I_{\text{sph}}^{(n)}$ and $L_{\text{sph}}^{(n)}$ denote, respectively, the moment of inertia and angular momentum of the sphere, defined by

$$I_{\text{sph}}^{(n)} = \int_{\Omega_{\text{sph}}} \rho_0 \left| \hat{\boldsymbol{x}}^{(n)} \times \boldsymbol{e}_y \right|^2 dV, \quad L_{\text{sph}}^{(n)} = -\int_{\Omega_{\text{sph}}} \rho_0 \left(\hat{\boldsymbol{x}}^{(n)} \times \hat{\boldsymbol{v}}^{(n)} \right) \cdot \boldsymbol{e}_y \, dV. \tag{28}$$

By inserting Eqs. (27) and (28) into Eq. (16), the objective function for the TO problem is obtained. The material parameters for the design domain $\Omega_0 = \Omega_{\text{ds}} \cup \Omega_{\text{nds}}$ are assigned the properties of Material 1 listed in Table 1, while those of the spherical contacting object Ω_0' follow the properties of Material 2.

Fig. 9 summarizes the TO results for braking structures designed to attenuate the rotational motion of a spinning spherical body. Panels (a)–(c) present three cases with different friction coefficients, $\mu_f = 0.3$, 0.4, and 0.5, each showing a time series of the dynamic contact process. The colormap on the sphere illustrates the magnitude of the relative velocity field $\hat{\boldsymbol{v}}$, which quantitatively represents the remaining rotational motion. In case (a), the optimized structure and the elastic sphere exhibit their strongest mutual engagement at approximately $t = 3.0$ ms. At this moment, the compliant contact surface of the brake structure undergoes significant deformation, effectively wrapping around the sphere. This "embracing" deformation is mechanically highly effective: by substantially increasing

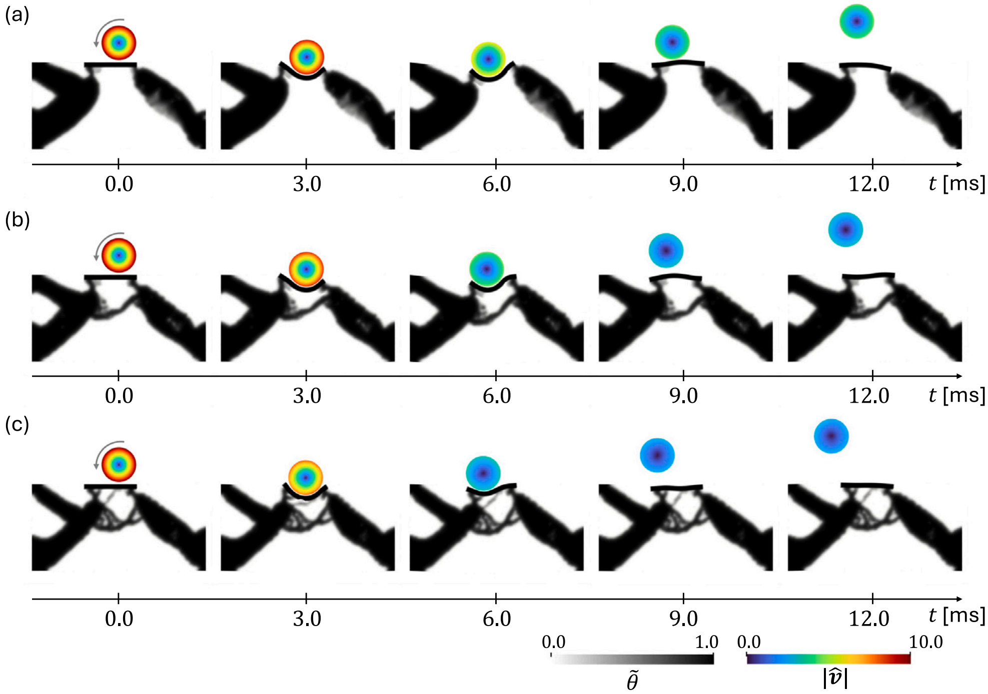

Fig. 9. Snapshots of deformation of optimized 2D brake structures for different friction coefficients: (a) $\mu_f = 0.3$, (b) $\mu_f = 0.4$, and (c) $\mu_f = 0.5$. The filtered design variable $\tilde{\theta}$ is used for visualization of the optimal structure. The sphere is colored according to the norm of the dimensionless relative velocity field $\bar{\boldsymbol{v}} = \hat{\boldsymbol{v}}/v_{\max}$, where $v_{\max} = R\omega_{\text{init}}$ is the circumferential velocity at the initial time. (For interpretation of the references to color in this figure legend, the reader is referred to the web version of this article.)

the interfacial contact area and generating larger normal contact forces, the structure amplifies the available frictional resistance. Since frictional dissipation scales with both normal pressure and the relative sliding distance, this configuration maximizes the rate at which angular momentum is removed from the rotating sphere. By $t = 6.0$ ms, the contact is still maintained, and the colormap clearly reveals a substantial reduction in rotational velocity. This demonstrates that sustained, conformal contact—rather than a brief impact—is critical for efficient braking performance. Subsequently, at $t = 9.0$ ms, the previously deflected internal beam begins to return toward its undeformed configuration, and by $t = 12.0$ ms the sphere and structure have fully separated.

The resulting optimal structures show substantial variations depending on the friction coefficient. Indeed, these differences become evident when comparing the pre-contact configurations at $t = 0$ in Figs. (a), (b), and (c). Nevertheless, despite the geometric variations introduced by different values of μ_f, the characteristic phases of the contact dynamics—initial impact, wrap-around engagement, sustained frictional braking, and eventual separation—appear consistently in all cases. Overall, these results indicate that an effective strategy for dissipating rotational energy using a compliant braking structure is to exploit deformation modes that allow the structure to wrap around and embrace the rotating body. By doing so, the structure leverages increased contact area, enhanced normal loading, and extended frictional interaction, thereby maximizing frictional energy dissipation and achieving rapid rotational deceleration.

4.4. An optimal braking structure for a rotating spherical object: 3D case

We finally extend the TO problem for the braking structure to a fully 3D setting. The geometric configuration and boundary conditions are shown in Fig. 10(a), where small square regions at the four corners are fully constrained as Dirichlet boundaries. As illustrated in Fig. 10(b), three cases are considered with different initial rotation axes of the sphere, namely $\boldsymbol{e}_x$, $\boldsymbol{e}_y$, and $\boldsymbol{e}_z$. The friction coefficient is fixed at $\mu_f = 0.3$ for all cases, and all other analysis conditions—including the objective function—follow the two-dimensional formulation, except that the rotation axis in Eq. (27) is replaced by the corresponding axis for each case. At the top surface of the design domain Ω_{ds}, a rectangular non-design region is placed, whose initial in-plane extent is set equal to the sphere radius (10 mm) in all directions. For the rotation axis of $\boldsymbol{e}_y$ or $\boldsymbol{e}_x$, this region is enlarged by an additional 20 mm in one in-plane direction (resulting in a total extent of 30 mm) to accommodate the friction-induced horizontal motion of the sphere.

The resulting optimal structures are shown in Fig. 11, along with time-series snapshots of the dynamic contact process. Streamlines inside the sphere visualize the relative velocity field $\hat{\boldsymbol{v}}$, and the colormap indicates its magnitude, $|\hat{\boldsymbol{v}}|$. Across all rotation directions, the optimized structures reduce the sphere's rotational velocity through frictional contact, consistent with the mechanism

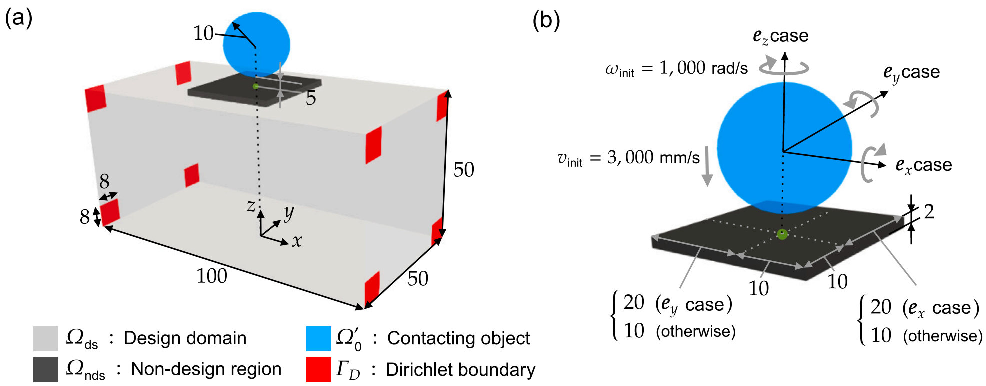

Fig. 10. (a) Simulation setup for the 3D optimal braking structure for a rotating spherical object. The non-design region Ω_0' is introduced to enhance the numerical stability of the TO analysis. (b) Dimensions of the rectangular non-design region at the top surface of the design domain $\Omega_{\rm ds}$.

identified in the two-dimensional study. Despite differences in rotation direction, each topology adapts to promote deformation modes that (i) enlarge the effective contact interface, (ii) generate substantial normal reaction forces, and (iii) sustain the duration of contact—three essential factors for maximizing frictional energy dissipation. In the $\boldsymbol{e}_x$ case (Fig. 11(a)), four beams extend from the lower corners of the end faces toward the contact region, providing compliant support that deforms to partially enclose the sphere. For $\boldsymbol{e}_y$ (Fig. 11(b)), the optimized geometry closely resembles the two-dimensional result in Fig. 9; columns extend from the Dirichlet boundaries on both end faces, enabling the structure to wrap around the sphere in an asymmetric manner. In the $\boldsymbol{e}_z$ case (Fig. 11(c)), the structure again forms columnar supports from the lower Dirichlet boundaries, facilitating multidirectional compression on the sphere and promoting efficient dissipation of angular momentum.

These three-dimensional results strongly reinforce the core design principle identified in the two-dimensional analysis: optimal braking structures consistently develop compliant deformation modes that wrap around or partially embrace the rotating sphere. This robust behavior across all rotation directions demonstrates that enabling controlled embracing deformation is a highly effective and broadly applicable strategy for compliant braking structures operating under frictional contact.

5. Conclusions

We developed a unified TO framework incorporating a hybrid MPM into a conventional finite element formulation. This framework enables the analysis of dynamic mechanical contact with friction, facilitating the optimal design of compliant structures subject to large deformations, evolving contact interfaces, and friction-induced energy dissipation—key characteristics of soft robotic and flexible mechanical systems. The conclusion of this study is summarized as follows:

1. We outlined the contact analysis based on the hybrid MPM proposed by Han et al. [45]. This method seamlessly integrates the strengths of FEM and MPM, offering several distinct advantages for complex contact problems: (i) It eliminates the need for explicit surface contact searches and subsequent force corrections, thereby simplifying the contact treatment; (ii) The FEM mesh discretization prevents numerical fracture under large deformation and enables an accurate total Lagrangian formulation; (iii) The use of FEM shape functions allows for the straightforward computation of surface normals, which are essential for contact algorithms. (iv) It is designed to suppress non-physical numerical adhesion and to enable Coulomb friction analysis through a stick–slip formulation by incorporating the relative motion between contacting interfaces during the MPM mapping step.
2. The conventional TO framework can be directly and seamlessly applied to the hybrid MPM because its mathematical structure is essentially identical to that of the standard FEM. To compute the sensitivities with respect to the design variable, we employed the adjoint method, with automatic differentiation efficiently implemented using the Taichi programming language. The design variables were subsequently updated iteratively using the method of moving asymptotes algorithm until convergence was achieved.
3. In the compliance minimization of a three-point bending configuration, we revealed a strong dependence of the optimal topology on both lateral indenter motion and interfacial friction. Specifically, the dynamically shifting contact location resulted in highly asymmetric material distribution and topology, with the most notable structural changes occurring near the indentation point. The successful extension of this analysis to three dimensions further confirmed the robustness and generality of the proposed method, demonstrating consistent structural adaptation even under multidirectional lateral loading.
4. The proposed TO framework was successfully applied to the design of optimal braking structures intended to suppress the rotational motion of a spinning elastic sphere. The optimized structures displayed a characteristic and mechanically advantageous behavior: they deformed to embrace the rotating sphere, thereby optimally enlarging the contact interface, increasing normal reaction forces, and prolonging frictional engagement. This "embracing" deformation mode—consistently

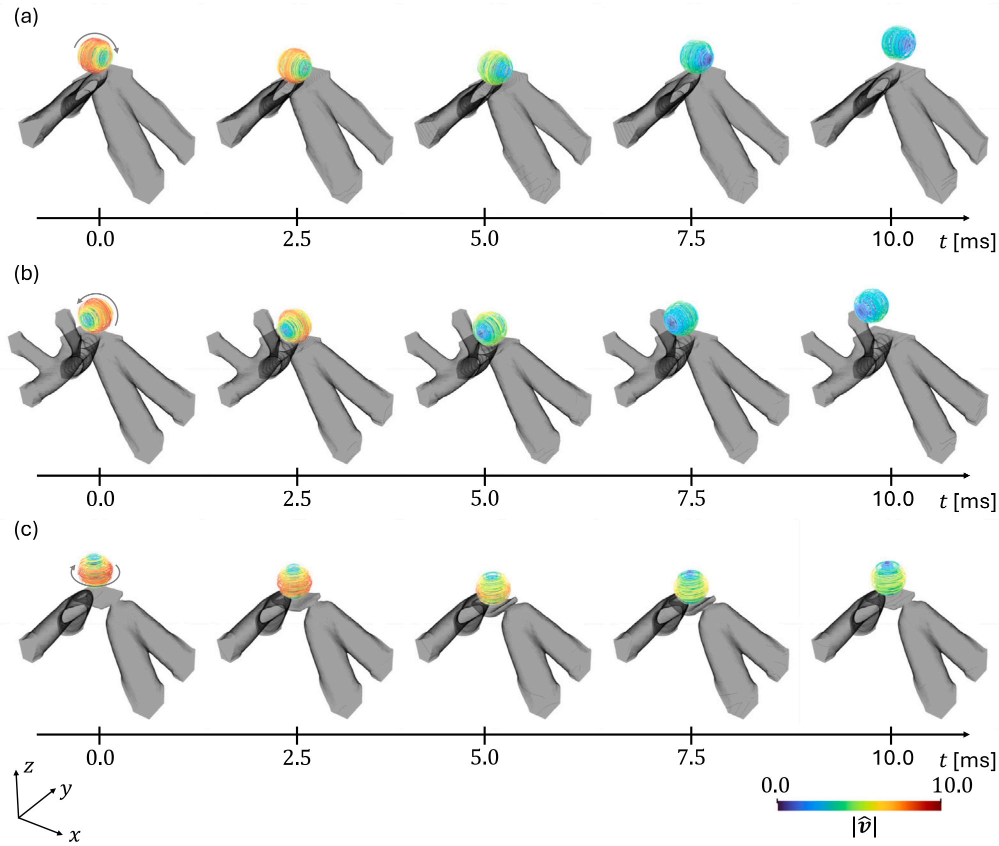

Fig. 11. Snapshots of the deformation of the optimal structures for different rotation axes: (a) e_x, (b) e_y, and (c) e_z. Inside the sphere, streamlines visualize the relative velocity field $\hat{\boldsymbol{v}}$, with colors indicating its magnitude with respect to the center-of-mass velocity. In all cases, the sphere progressively loses rotational speed due to frictional contact with the surrounding structure. (For interpretation of the references to color in this figure legend, the reader is referred to the web version of this article.)

observed in both two- and three-dimensional cases—maximizes frictional work and enables rapid dissipation of angular momentum. Generally, soft robots are defined as functional systems composed of highly flexible materials. Accordingly, the numerical examples presented in this study can be interpreted as representative models of such robotic components.

5. A primary limitation of the present framework lies in the restricted physical time scale governed by the time-integration scheme. Since the current Hybrid MPM is formulated using an explicit dynamic scheme, the maximum stable time step, $\Delta t_{\max}$, is strictly dictated by the FEM mesh size and the wave propagation speed within the elastic body. Furthermore, for optimization problems involving temporal evolution (Section 3.3), the necessity of storing the state variable history imposes additional constraints on the total number of time steps, N_T, due to computational memory limits. Consequently, the framework is currently limited to dynamic contact problems with a relatively short physical duration, $\Delta t_{\max} N_T$; indeed, all examples in Section 4 are restricted to durations of no more than 1.5×10^{-2} s. To overcome these bottlenecks, developing a Hybrid MPM based on an implicit dynamic scheme is a promising direction, as it would extend the accessible physical time range while maintaining the advantage of avoiding explicit contact detection.

The proposed framework substantially broadens the scope of TO by making it possible to directly utilize dynamic, frictional contact mechanics in structural design. This capability enables new design opportunities for advanced systems, including soft robotic components, energy-dissipating devices, and compliant mechanical systems operating under complex dynamic contact conditions.

CRediT authorship contribution statement

Isamu Hashiguchi: Writing – review & editing, Writing – original draft, Visualization, Validation, Software, Project administration, Methodology, Investigation, Formal analysis, Data curation, Conceptualization. **Jike Han:** Writing – review & editing, Writing – original draft, Supervision, Project administration, Methodology, Formal analysis, Conceptualization. **Shunsuke Kobayashi:** Writing – review & editing, Writing – original draft, Supervision, Project administration, Formal analysis. **Takamitsu Sasaki:** Methodology, Investigation, Formal analysis. **Ryuichi Tarumi:** Writing – review & editing, Writing – original draft, Supervision, Resources, Project administration, Funding acquisition.

Declaration of Generative AI and AI-assisted technologies in the writing process

During the preparation of this work the authors used ChatGPT in order to improve grammar and readability of the manuscript. After using this tool/service, the authors reviewed and edited the content as needed and take full responsibility for the content of the published article.

Declaration of competing interest

The authors declare that they have no known competing financial interests or personal relationships that could have appeared to influence the work reported in this paper.

Acknowledgments

This work was supported by JST PRESTO Grant Number JPMJPR1997, JST, the establishment of university fellowships towards the creation of science technology innovation, Grant Number JPMJFS2125, JSPS KAKENHI Grant Numbers JP23K17317, JP25K17528.

Appendix A. Filtering method for design variable

We employ the Helmholtz filter [66] to obtain a filtered design variable $\tilde{\theta}$ from the original design variable θ. Let $\delta\tilde{\theta}$ denote the test function associated with $\tilde{\theta}$. Then, the weak form of the governing equation for determining $\tilde{\theta}$ is expressed as

$$\int_{\Omega_{\mathrm{ds}}} \left((\tilde{\theta} - \theta)\delta\tilde{\theta} + r^2 \frac{\partial \tilde{\theta}}{\partial \boldsymbol{X}} \cdot \frac{\partial \delta\tilde{\theta}}{\partial \boldsymbol{X}} \right) dV = 0, \tag{A.1}$$

where r denotes the characteristic length defining the filtering radius, and in the present analysis, we set r equal to the mesh size. The design variables θ, $\tilde{\theta}$, and the test function $\delta\tilde{\theta}$ are approximated using FE discretization as

$$\theta(\boldsymbol{X}) \approx \sum_{\alpha\in\mathcal{N}_{\mathrm{FA}}} K_\alpha(\boldsymbol{X})\theta_\alpha, \quad \tilde{\theta}(\boldsymbol{X}) \approx \sum_{\alpha\in\mathcal{N}_{\mathrm{FA}}} K_\alpha(\boldsymbol{X})\tilde{\theta}_\alpha, \quad \delta\tilde{\theta}(\boldsymbol{X}) \approx \sum_{\alpha\in\mathcal{N}_{\mathrm{FA}}} K_\alpha(\boldsymbol{X})\delta\tilde{\theta}_\alpha, \tag{A.2}$$

Substituting these approximations into the weak formulation in Eq. (A.1) yields the following linear discrete system:

$$\boldsymbol{A}\tilde{\boldsymbol{\theta}} = \boldsymbol{B}\boldsymbol{\theta}, \tag{A.3}$$

where $\boldsymbol{\theta}$ and $\tilde{\boldsymbol{\theta}}$ denote global vectors collecting the nodal values in the design domain Ω_{ds}. The matrices $\boldsymbol{A}$ and $\boldsymbol{B}$ are symmetric, and their entries are given by

$$A_{\alpha\beta} = \int_{\Omega_{\mathrm{ds}}} \left(K_\alpha K_\beta + r^2 \frac{\partial K_\alpha}{\partial \boldsymbol{X}} \cdot \frac{\partial K_\beta}{\partial \boldsymbol{X}} \right) dV, \quad B_{\alpha\beta} = \int_{\Omega_{\mathrm{ds}}} K_\alpha K_\beta dV. \tag{A.4}$$

The filtered variable $\tilde{\theta}$ obtained from the operation is used to interpolate the local material parameters and the strain energy density (see Appendix B). These interpolated quantities are then used in the structural analysis and, consequently, in the evaluation of the objective function F via the time-integration operator $\boldsymbol{\mathcal{T}}$. This implies that the Lagrangian $\mathcal{L}$ for the sensitivity analysis depends implicitly on the filtered variable $\tilde{\theta}$. According to the chain rule, we have

$$\frac{\partial \mathcal{L}}{\partial \boldsymbol{\theta}} = \frac{\partial \mathcal{L}}{\partial \tilde{\boldsymbol{\theta}}} \frac{\partial \tilde{\boldsymbol{\theta}}}{\partial \boldsymbol{\theta}} = \left(\frac{\partial \tilde{\boldsymbol{\theta}}}{\partial \boldsymbol{\theta}} \right)^T \frac{\partial \mathcal{L}}{\partial \tilde{\boldsymbol{\theta}}} = \left(\boldsymbol{A}^{-1}\boldsymbol{B} \right)^T \frac{\partial \mathcal{L}}{\partial \tilde{\boldsymbol{\theta}}} = \boldsymbol{B}\boldsymbol{A}^{-1} \frac{\partial \mathcal{L}}{\partial \tilde{\boldsymbol{\theta}}}. \tag{A.5}$$

For the actual computation, we first evaluate the sensitivity of the Lagrangian with respect to the filtered design variable, $\partial\mathcal{L}/\partial\tilde{\theta}$, using Eq. (A.3) together with the automatic differentiation provided by Taichi. We then obtain the sensitivity with respect to the unfiltered design variable $\partial\mathcal{L}/\partial\theta$ using Eq. (A.5).

Appendix B. Elastic constitutive law for topology optimization

To ensure numerical stability under large deformations, we adopt the energy-interpolation-based constitutive model proposed by Wang et al. [67]. This method implements a switching constitutive law based on the design variable θ: a hyperelastic model (which includes both geometric and material nonlinearity) is employed in the elastic (solid) region ($\theta \approx 1$), while a simple linear elastic model is used in the void region ($\theta \approx 0$). This strategy is characterized by its ability to effectively suppress numerical instabilities caused by excessive mesh distortion in low-stiffness regions. The strain energy density function in this method is defined as:

$$\varphi(\boldsymbol{u}) = \varphi_N(\gamma_\varphi \boldsymbol{u}) - \varphi_L(\gamma_\varphi \boldsymbol{u}) + \varphi_L(\boldsymbol{u}), \tag{B.1}$$

where γ_φ is a scalar switch and φ_N and φ_L denote the strain–energy densities of a Neo-Hookean hyperelastic material and a linear elastic material, respectively. They are given by

$$\varphi_N(\boldsymbol{u}) = \frac{\mu}{2} \left(\mathrm{tr}\left(\boldsymbol{F}^T \boldsymbol{F} \right) - d \right) - \mu \log(J) + \frac{\lambda}{2} \log^2(J), \tag{B.2}$$

Table C.1
Average computational time per optimization iteration for each case presented in Section 3.

Compl. min., 2D	Compl. min., 3D	Brake, 2D	Brake, 3D
144.73 s	124.69 s	140.62 s	62.49 s

$$\varphi_L(\boldsymbol{u}) = \mu\boldsymbol{\epsilon} : \boldsymbol{\epsilon} + \frac{\lambda}{2}(\mathrm{tr}\boldsymbol{\epsilon})^2, \tag{B.3}$$

where $\boldsymbol{\epsilon}$ denotes the linear strain tensor, which is expressed in terms of the deformation gradient tensor $\boldsymbol{F}$ as $\boldsymbol{\epsilon} = \left(\boldsymbol{F} + \boldsymbol{F}^T - 2\boldsymbol{I}\right)/2$. The Lamé parameters λ and μ are related to Young's modulus E and Poisson's ratio ν by

$$\lambda = \frac{E\nu}{(1+\nu)(1-2\nu)}, \quad \mu = \frac{E}{2(1+\nu)}. \tag{B.4}$$

Young's modulus $E = E(\tilde{\theta})$ is taken as a function of the filtered design variable $\tilde{\theta}$, and is interpolated using the Solid Isotropic Material with Penalization (SIMP) method [68] as

$$E = \left(\left(1-\gamma_{\min}\right)\tilde{\theta}^p + \gamma_{\min}\right)E_0, \tag{B.5}$$

where E_0 is the Young's modulus in the solid region, and $\gamma_{\min}$ is the minimum Young's modulus ratio between the void region and the solid region. p is the SIMP penalization exponent that controls how strongly intermediate densities are discouraged. Similarly, the mass density is interpolated according to Eq. (B.5) using the solid density ρ_0. From the interpolated strain energy density function given in Eq. (B.1), the first Piola–Kirchhoff stress is derived as follows:

$$\boldsymbol{P} = \gamma_\varphi \boldsymbol{P}_N(\gamma_\varphi \boldsymbol{u}) + \left(1-\gamma_\varphi^2\right)\boldsymbol{P}_L(\boldsymbol{u}), \tag{B.6}$$

where $\boldsymbol{P}_N$ and $\boldsymbol{P}_L$ denote the first Piola–Kirchhoff stresses obtained from the Neo-Hookean hyperelastic model and the linear elastic model, respectively.

To achieve a smooth transition of the energy interpolation in Eq. (B.1), the constitutive parameter $\gamma_\varphi = \gamma_\varphi(\tilde{\theta})$ is continuously varied with respect to the filtered design variable, and is expressed using the Heaviside projection as follows:

$$\gamma_\varphi = \frac{\tanh(\beta_\varphi\omega_\varphi) + \tanh(\beta_\varphi(\tilde{\theta}^p - \omega_\varphi))}{\tanh(\beta_\varphi\omega_\varphi) + \tanh(\beta_\varphi(1-\omega_\varphi))}. \tag{B.7}$$

Here, β_φ and ω_φ denote the parameters controlling the steepness of the transition and the threshold value representing the transition point, respectively.

Appendix C. Computational details

As shown in Section 2, the contact analysis based on the MPM mapping operation consists of simple summation operations. Therefore, the algorithm is well suited for GPU parallelization. In this study, to take advantage of this feature, we implemented the program using Taichi [60,61], a Python-based programming framework that enables straightforward GPU parallel computing. The computations were performed using an NVIDIA GeForce RTX 3090. The GPU is equipped with 10,496 CUDA cores and 24 GB of GPU memory. Double precision was adopted for all computations. For future studies on topology optimization involving dynamic contact, Table C.1 summarizes the average computational time per iteration for each case presented in Section 4. In all cases, the computation for a single iteration was completed within 3 min.

Appendix D. Mesh-resolution dependence of the optimization structures

The effect of FE mesh size on the optimized structure is investigated using the compliance minimization of the three-point bending problem illustrated in Fig. 3. Based on the reference mesh size from the main numerical example (Fig. 4), two additional cases with double and half the resolution are introduced; specifically, mesh sizes of 2 mm, 1 mm, and 0.5 mm are examined. To ensure a consistent evaluation of the contact effects associated with the MPM mapping, the Eulerian grid spacing is fixed at 1 mm. Correspondingly, the number of CPs along each mesh boundary is adjusted to maintain a uniform spatial density of CPs across all cases, as depicted in Fig. D.1(a). The same mesh configurations are applied to the supports and the indenter. The height of the non-design region is set to 2 mm to ensure divisibility by each mesh size. Furthermore, the filter radius r in Eq. (A.1) is fixed at 2 mm to ensure the filtering remains effective even for the coarsest mesh. The indenter is constrained to vertical motion ($\bar{u}_x = 0$, $\bar{u}_z = 10$ mm) with the friction coefficient set to $\mu_f = 0$. All other computational parameters follow the settings described in Section 4.1.

The resulting optimal structures are presented in Fig. D.1(b). In all cases, the optimized topologies maintain left–right symmetry, exhibiting similar overall structural features despite minor variations in detailed connectivity. Table D.2 summarizes the objective function values for the initial and optimized structures. The significant reduction in the objective function across all cases confirms the effectiveness of the optimization framework for this minimization problem. Furthermore, the degree of improvement is consistent across the different mesh resolutions. While the objective function value tends to increase as the mesh is refined, this trend is attributed to the alleviation of shear locking [69,70] rather than any inherent flaw in the proposed method. This interpretation is supported by the fact that this tendency is consistently observed in both the initial and optimized configurations. Given the similarity of the obtained topologies and the consistency of the performance metrics, we conclude that the present method demonstrates high reproducibility and stable behavior with respect to mesh resolution.

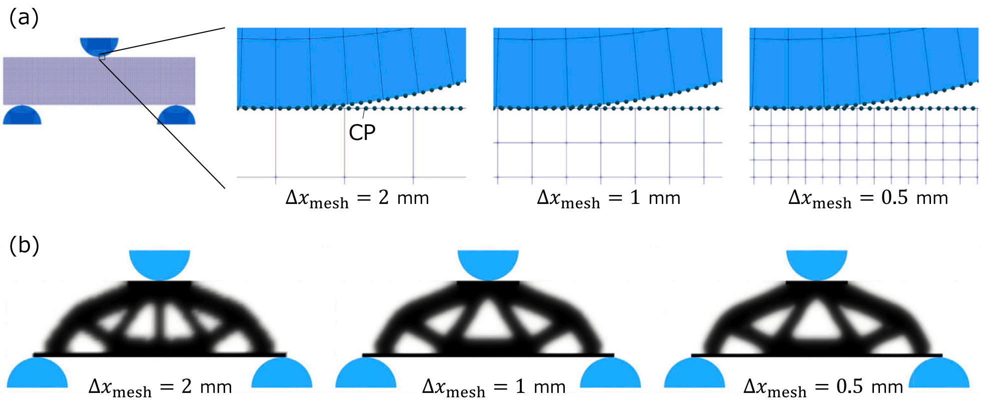

Fig. D.1. (a) Mesh configurations of the three cases considered in the mesh-resolution study, with a magnified view near the contact boundary between the indenter and the design domain. The number of CPs is set to be identical in all cases. (b) Optimized structures for each case..

Table D.2
Objective function values for the initial structure ($\theta = 0.5$) and the optimized structure in each case shown in Fig. D.1(b).

Δx_{mesh}	2 mm	1 mm	0.5 mm
Initial structure [J]	−2.577	−2.413	−2.318
Optimal structure [J]	−7.539	−7.256	−7.061

Data availability

The data and source code associated with this study are publicly available at [71].

References

[1] D. Rus, M. Tolley, Design, fabrication and control of soft robots, Nature 521 (2015) 467–475, http://dx.doi.org/10.1038/nature14543.
[2] C. Laschi, B. Mazzolai, M. Cianchetti, Soft robotics: Technologies and systems pushing the boundaries of robot abilities, Sci. Robot. 1 (2016) eaah3690, http://dx.doi.org/10.1126/scirobotics.aah3690.
[3] H. Yin, W. Zhang, L. Zhu, F. Meng, J. Liu, G. Wen, Review on lattice structures for energy absorption properties, Compos. Struct. 304 (2023) 116397, http://dx.doi.org/10.1016/j.compstruct.2022.116397.
[4] P. Blake, O. Hawary, K. Myronidis, F. Pinto, C. Fallon, 3D-auxetic elastomeric cellular structures for impact protection, Int. J. Prot. Struct. (2024) http://dx.doi.org/10.1177/20414196241284296.
[5] J. Shintake, V. Cacucciolo, D. Floreano, H. Shea, Soft robotic grippers, Adv. Mater. 30 (2018) 1707035, http://dx.doi.org/10.1002/adma.201707035.
[6] H. Wenkai, J. Xiao, Z. Xu, A variable structure pneumatic soft robot, Sci. Rep. 10 (2020) http://dx.doi.org/10.1038/s41598-020-75346-5.
[7] M.P. Bendsøe, N. Kikuchi, Generating optimal topologies in structural design using a homogenization method, Comput. Methods Appl. Mech. Engrg. 71 (2) (1988) 197–224, http://dx.doi.org/10.1016/0045-7825(88)90086-2.
[8] T. Buhl, C.B.W. Pedersen, O. Sigmund, Stiffness design of geometrically nonlinear structures using topology optimization, Struct. Multidiscip. Optim. 19 (2000) 93–104, http://dx.doi.org/10.1007/s001580050089.
[9] T.E. Bruns, D.A. Tortorelli, Topology optimization of non-linear elastic structures and compliant mechanisms, Comput. Methods Appl. Mech. Engrg. 190 (2001) 3443–3459, http://dx.doi.org/10.1016/S0045-7825(00)00278-4.
[10] Z. Kang, Y. Luo, Non-probabilistic reliability-based topology optimization of geometrically nonlinear structures using convex models, Comput. Methods Appl. Mech. Engrg. 198 (2009) 3228–3238, http://dx.doi.org/10.1016/j.cma.2009.06.001.
[11] Y. Luo, M.Y. Wang, Z. Kang, Topology optimization of geometrically nonlinear structures based on an additive hyperelasticity technique, Comput. Methods Appl. Mech. Engrg. 286 (2015) 422–441, http://dx.doi.org/10.1016/j.cma.2014.12.023.
[12] M. Wallin, V. Jönsson, E. Wingren, Topology optimization based on finite strain plasticity, Struct. Multidiscip. Optim. 54 (4) (2016) 783–793, http://dx.doi.org/10.1007/s00158-016-1435-0.
[13] A.L.F. da Silva, R.A. Salas, E.C.N. Silva, J.N. Reddy, Topology optimization of fibers orientation in hyperelastic composite material, Compos. Struct. 231 (2020) 111488, http://dx.doi.org/10.1016/j.compstruct.2019.111488.
[14] X.S. Zhang, H. Chi, Z. Zhao, Topology optimization of hyperelastic structures with anisotropic fiber reinforcement under large deformations, Comput. Methods Appl. Mech. Engrg. 378 (2021) 113496, http://dx.doi.org/10.1016/j.cma.2020.113496.
[15] J. Han, Y. Yamakawa, K. Izui, S. Nishiwaki, K. Terada, Multi-material topology optimization based on finite strain subloading surface nonlocal elastoplasticity, Comput. Methods Appl. Mech. Engrg. 442 (2025) 118038, http://dx.doi.org/10.1016/j.cma.2025.118038.
[16] S. Min, N. Kikuchi, Y.C. Park, S. Kim, S. Chang, Optimal topology design of structures under dynamic loads, Struct. Optim. 17 (2) (1999) 208–218, http://dx.doi.org/10.1007/BF01195945.
[17] H.H. Jang, H.A. Lee, J.Y. Lee, G.J. Park, Dynamic response topology optimization in the time domain using equivalent static loads, AIAA J. 50 (1) (2012) 226–234, http://dx.doi.org/10.2514/1.J051256.
[18] J. Zhao, C. Wang, Topology optimization for minimizing the maximum dynamic response in the time domain using aggregation functional method, Comput. Struct. 190 (2017) 41–60, http://dx.doi.org/10.1016/j.compstruc.2017.05.002.

[19] R. Behrou, J.K. Guest, Topology optimization for transient response of structures subjected to dynamic loads, in: Proc. 18th AIAA/ISSMO Multidisciplinary Analysis and Optimization Conference AIAA AVIATION Forum, Paper AIAA 2017-3657, 2017, http://dx.doi.org/10.2514/6.2017-3657.
[20] G.H. Yoon, Topology optimization for nonlinear dynamic problem with multiple materials and material-dependent boundary condition, Finite Elem. Anal. Des. 47 (7) (2011) 753–763, http://dx.doi.org/10.1016/j.finel.2011.02.006.
[21] S. Ogawa, T. Yamada, Topology optimization of dynamic problems based on finite deformation theory, Internat. J. Numer. Methods Engrg. 122 (17) (2021) 4486–4506, http://dx.doi.org/10.1002/nme.6710.
[22] H. Kristiansen, K. Poulios, N. Aage, Topology optimization of structures in transient impacts with Coulomb friction, Internat. J. Numer. Methods Engrg. 122 (18) (2021) 5053–5075, http://dx.doi.org/10.1002/nme.6756.
[23] N.D. Mankame, G.K. Ananthasuresh, Topology optimization for synthesis of contact-aided compliant mechanisms using regularized contact modeling, Comput. Struct. 82 (2004) 1267–1290, http://dx.doi.org/10.1016/j.compstruc.2004.02.024.
[24] E.A. Fancello, Topology optimization for minimum mass design considering local failure constraints and contact boundary conditions, Struct. Multidiscip. Optim. 32 (2006) 229–240, http://dx.doi.org/10.1007/s00158-006-0019-9.
[25] N. Strömberg, A. Klarbring, Topology optimization of structures in unilateral contact, Struct. Multidiscip. Optim. 41 (2010) 57–64, http://dx.doi.org/10.1007/s00158-009-0407-z.
[26] M. Lawry, K. Maute, Level set topology optimization of problems with sliding contact interfaces, Struct. Multidiscip. Optim. 52 (2015) 1107–1119, http://dx.doi.org/10.1007/s00158-015-1301-5.
[27] C. Niu, W. Zhang, T. Gao, Topology optimization of elastic contact problems with friction using efficient adjoint sensitivity analysis with load increment reduction, Comput. Struct. 238 (2020) 106296, http://dx.doi.org/10.1016/j.compstruc.2020.106296.
[28] H. Kristiansen, K. Poulios, N. Aage, Topology optimization for compliance and contact pressure distribution in structural problems with friction, Comput. Methods Appl. Mech. Engrg. 364 (2020) 112915, http://dx.doi.org/10.1016/j.cma.2020.112915.
[29] B.V.S. Nagendra Reddy, S.V. Naik, A. Saxena, Systematic synthesis of large displacement contact-aided monolithic compliant mechanisms, J. Mech. Des. 134 (2012) http://dx.doi.org/10.1115/1.4005326.
[30] Y. Luo, M. Li, Z. Kang, Topology optimization of hyperelastic structures with frictionless contact supports, Int. J. Solids Struct. 81 (2016) 373–382, http://dx.doi.org/10.1016/j.ijsolstr.2015.12.018.
[31] F. Fernandez, M.A. Puso, J. Solberg, D.A. Tortorelli, Topology optimization of multiple deformable bodies in contact with large deformations, Comput. Methods Appl. Mech. Engrg. 371 (2020) 113288, http://dx.doi.org/10.1016/j.cma.2020.113288.
[32] G.L. Bluhm, O. Sigmund, K. Poulios, Internal contact modeling for finite strain topology optimization, Comput. Mech. 67 (2021) 1099–1114, http://dx.doi.org/10.1007/s00466-021-01974-x.
[33] A.H. Frederiksen, A. Dalklint, O. Sigmund, K. Poulios, Improved third medium formulation for 3D topology optimization with contact, Comput. Methods Appl. Mech. Engrg. 436 (2025) 117595, http://dx.doi.org/10.1016/j.cma.2024.117595.
[34] J. Huang, J. Liu, Strength constrained topology optimization of hyperealstic structures with large deformation-induced frictionless contact, Appl. Math. Model. 126 (2024) 67–84, http://dx.doi.org/10.1016/j.apm.2023.10.032.
[35] N.G. Burago, V.N. Kukudzhanov, A review of contact algorithms, Mech. Solids 40 (1) (2005) 35–71.
[36] P. Wriggers, Computational Contact Mechanics, second ed., Springer, Berlin, Heidelberg, 2006, http://dx.doi.org/10.1007/978-3-540-32609-0.
[37] P. Wriggers, J. Schröder, A. Schwarz, A finite element method for contact using a third medium, Comput. Mech. 52 (4) (2013) 837–847, http://dx.doi.org/10.1007/s00466-013-0848-5.
[38] A.H. Frederiksen, O. Sigmund, K. Poulios, Topology optimization of self-contacting structures, Comput. Mech. 73 (4) (2024) 967–981, http://dx.doi.org/10.1007/s00466-023-02396-7.
[39] D. Sulsky, Z. Chen, H. Schreyer, A particle method for history-dependent materials, Comput. Methods Appl. Mech. Engrg. 118 (1) (1994) 179–196, http://dx.doi.org/10.1016/0045-7825(94)90112-0.
[40] Y. Sato, H. Kobayashi, C. Yuhn, A. Kawamoto, T. Nomura, N. Kikuchi, Topology optimization of locomoting soft bodies using material point method, Struct. Multidiscip. Optim. 66 (2023) 50, http://dx.doi.org/10.1007/s00158-023-03502-2.
[41] H. Kobayashi, F. Gholami, S.M. Montgomery, M. Tanaka, L. Yue, C. Yuhn, Y. Sato, A. Kawamoto, H.J. Qi, T. Nomura, Computational synthesis of locomotive soft robots by topology optimization, Sci. Adv. 10 (30) (2024) eadn6129, http://dx.doi.org/10.1126/sciadv.adn6129.
[42] C. Yuhn, Y. Sato, H. Kobayashi, A. Kawamoto, T. Nomura, 4D topology optimization: Integrated optimization of the structure and self-actuation of soft bodies for dynamic motions, Comput. Methods Appl. Mech. Engrg. 414 (2023) 116187, http://dx.doi.org/10.1016/j.cma.2023.116187.
[43] Y. Sato, C. Yuhn, H. Kobayashi, A. Kawamoto, T. Nomura, Computational co-design of structure and feedback controller for locomoting soft robots, Struct. Multidiscip. Optim. (2024) http://dx.doi.org/10.2139/ssrn.4904034.
[44] L. Wang, Co-design of magnetic soft robots with large deformation and contacts via material point method and topology optimization, Comput. Methods Appl. Mech. Engrg. 445 (2025) 118205, http://dx.doi.org/10.1016/j.cma.2025.118205.
[45] X. Han, T.F. Gast, Q. Guo, S. Wang, C. Jiang, J. Teran, A hybrid material point method for frictional contact with diverse materials, Proc. ACM Comput. Graph. Interact. Tech. 2 (2) (2019) http://dx.doi.org/10.1145/3340258.
[46] V.P. Nguyen, A. de Vaucorbeil, C. Nguyen-Thanh, T.K. Mandal, A generalized particle in cell method for explicit solid dynamics, Comput. Methods Appl. Mech. Engrg. 371 (2020) 113308, http://dx.doi.org/10.1016/j.cma.2020.113308.
[47] S.G. Bardenhagen, J.U. Brackbill, D. Sulsky, The material-point method for granular materials, Comput. Methods Appl. Mech. Engrg. 187 (3) (2000) 529–541, http://dx.doi.org/10.1016/S0045-7825(99)00338-2.
[48] S. Bardenhagen, J. Guilkey, K. Roessig, J. Brackbill, W. Witzel, J. Foster, An improved contact algorithm for the material point method and application to stress propagation in granular material, Comput. Model. Eng. Sci. 2 (4) (2001) 509–522, http://dx.doi.org/10.3970/cmes.2001.002.509.
[49] S. Bardenhagen, G. Smith, Generalized contact and improved frictional heating in the material point method, Comput. Part. Mech. 5 (2017) http://dx.doi.org/10.1007/s40571-017-0168-1.
[50] R. Alberdi, K. Khandelwal, Bi-material topology optimization for energy dissipation with inertia and material rate effects under finite deformations, Finite Elem. Anal. Des. 164 (2019) 18–41, http://dx.doi.org/10.1016/j.finel.2019.06.003.
[51] F. Tian, J. Zeng, X. Tang, T. Xu, L. Li, A dynamic phase field model with no attenuation of wave speed for rapid fracture instability in hyperelastic materials, Int. J. Solids Struct. 202 (2020) 685–698, http://dx.doi.org/10.1016/j.ijsolstr.2020.07.004.
[52] S.R. Wu, Lumped mass matrix in explicit finite element method for transient dynamics of elasticity, Comput. Methods Appl. Mech. Engrg. 195 (44) (2006) 5983–5994, http://dx.doi.org/10.1016/j.cma.2005.10.008.
[53] E. Hinton, T. Rock, O.C. Zienkiewicz, A note on mass lumping and related processes in the finite element method, Earthq. Eng. Struct. Dyn. 4 (3) (1976) 245–249, http://dx.doi.org/10.1002/eqe.4290040305.
[54] P. Huang, X. Zhang, S. Ma, X. Huang, Contact algorithms for the material point method in impact and penetration simulation, Internat. J. Numer. Methods Engrg. 85 (4) (2011) 498–517, http://dx.doi.org/10.1002/nme.2981.
[55] J.M. Carbonell, E. Oñate, B. Suárez, Modeling of ground excavation with the particle Finite-Element method, J. Eng. Mech. 136 (4) (2010) 455–463, http://dx.doi.org/10.1061/(ASCE)EM.1943-7889.0000086.
[56] E.C. Hooijkamp, F.v. Keulen, Topology optimization for linear thermo-mechanical transient problems: Modal reduction and adjoint sensitivities, Internat. J. Numer. Methods Engrg. 113 (8) (2018) 1230–1257, http://dx.doi.org/10.1002/nme.5635.

[57] A. Sadeghirad, R.M. Brannon, J. Burghardt, A convected particle domain interpolation technique to extend applicability of the material point method for problems involving massive deformations, Internat. J. Numer. Methods Engrg. 86 (12) (2011) 1435–1456, http://dx.doi.org/10.1002/nme.3110.
[58] A. Sadeghirad, R. Brannon, J. Guilkey, Second-order convected particle domain interpolation (CPDI2) with enrichment for weak discontinuities at material interfaces, Internat. J. Numer. Methods Engrg. 95 (11) (2013) 928–952, http://dx.doi.org/10.1002/nme.4526.
[59] T. Lauß, S. Oberpeilsteiner, W. Steiner, K. Nachbagauer, The discrete adjoint method for parameter identification in multibody system dynamics, Multibody Syst. Dyn. 42 (4) (2018) 397–410, http://dx.doi.org/10.1007/s11044-017-9600-9.
[60] Y. Hu, L. Anderson, T.-M. Li, Q. Sun, N. Carr, J. Ragan-Kelley, F. Durand, DiffTaichi: Differentiable programming for physical simulation, ICLR (2020).
[61] Y. Hu, T.-M. Li, L. Anderson, J. Ragan-Kelley, F. Durand, Taichi: A language for high-performance computation on spatially sparse data structures, ACM Trans. Graph. 38 (6) (2019) http://dx.doi.org/10.1145/3355089.3356506.
[62] K. Svanberg, The method of moving asymptotes—A new method for structural optimization, Internat. J. Numer. Methods Engrg. 24 (1987) 359–373, http://dx.doi.org/10.1002/nme.1620240207.
[63] A. Deetman, GCMMA-MMA-python: Python implementation of the method of moving asymptotes, Zenodo (2025) http://dx.doi.org/10.5281/zenodo.15459165.
[64] X. Zhang, G. Duan, Y. Fang, X. Yin, W. Li, Topology optimization based on the improved high-order RAMP interpolation model and bending properties research for curved square honeycomb sandwich structures, Compos. Struct. 351 (2025) 118643, http://dx.doi.org/10.1016/j.compstruct.2024.118643.
[65] C. O'Shaughnessy, E. Masoero, P.D. Gosling, Topology optimization using the discrete element method. Part 1: Methodology, validation, and geometric nonlinearity, Meccanica 57 (6) (2022) 1213–1231, http://dx.doi.org/10.1007/s11012-022-01493-w.
[66] B. Lazarov, O. Sigmund, Filters in topology optimization based on Helmholtz-type differential equations, Internat. J. Numer. Methods Engrg. 86 (2011) 765–781, http://dx.doi.org/10.1002/nme.3072.
[67] F. Wang, B.S. Lazarov, O. Sigmund, J.S. Jensen, Interpolation scheme for fictitious domain techniques and topology optimization of finite strain elastic problems, Comput. Methods Appl. Mech. Engrg. 276 (2014) 453–472, http://dx.doi.org/10.1016/j.cma.2014.03.021.
[68] M. Bendsøe, Optimal shape design as a material distribution problem, Struct. Optim. 1 (1989) 193–202, http://dx.doi.org/10.1007/BF01650949.
[69] J.C. Simo, M.S. Rifai, A class of mixed assumed strain methods and the method of incompatible modes, Internat. J. Numer. Methods Engrg. 29 (8) (1990) 1595–1638, http://dx.doi.org/10.1002/nme.1620290802.
[70] J. Simo, F. Armero, R. Taylor, Improved versions of assumed enhanced strain tri-linear elements for 3D finite deformation problems, Comput. Methods Appl. Mech. Engrg. 110 (3) (1993) 359–386, http://dx.doi.org/10.1016/0045-7825(93)90215-J.
[71] I. Hashiguchi, Code and data for "A unified topology optimization framework for dynamic contact and friction via hybrid MPM", Mendeley Data V1 (2026) http://dx.doi.org/10.17632/srwmy6md4g.1.